Psychedelic 5-HT_{2A} receptor agonism: neuronal signatures and altered neurovascular coupling.

Jonah A. Padawer-Curry[1,2], Abraham Z. Snyder[2,3], Annie R. Bice[2], Xiaodan Wang[2,4], Ginger E. Nicol[3], Jordan G. McCall[5*], Joshua S. Siegel[3*], Adam Q. Bauer[1, 2,4*]

Imaging Science Program[1], Department of Radiology[2], Department of Psychiatry[3], Department of Biomedical Engineering[4], Department of Anesthesiology[5], Washington University in St. Louis, St. Louis, MO.

*These principal investigators contributed equally

Abstract
Psychedelics are attractive potential therapeutic agents for treatment resistant depression due to their rapid and sustained effects. These effects have been largely attributed to serotonin (5-hydroxytryptamine) receptor agonism, especially at the 5-HT_{2A} receptor (5-HT_{2A}R). Recent human functional neuroimaging studies report dramatic 5-HT_{2A}R-dependent changes in behavior and functional network organization that presumably reflect neuromodulatory effects. However, serotonin also has potent vasoactive effects that have not been assessed in prior imaging studies of classic (*i.e.*, 5-HT_{2A}R agonists) psychedelics. We assessed the neural, hemodynamic, and neurovascular coupling (NVC) effects of the hallucinogenic 5-HT_{2A} receptor agonist, 2,5-Dimethoxy-4-iodoamphetamine (DOI), using wide-field optical imaging (WFOI) in mice during both awake, whisker stimulation and under awake, resting-state conditions. Under both task and resting-state conditions, DOI narrowed hemodynamic response functions and enhanced transduction of neuronal activity in the delta band. These effects were regionally specific and strongest in association regions. Co-administration of DOI and 5-HT_{2a}R antagonist, MDL100907, reversed the effects of DOI on NVC. These DOI-induced NVC alterations imply a dissociation between neuronal versus hemodynamic signals and emphasize the need to consider the neurovascular effects of psychedelics when interpreting hemodynamic measures of neuronal activity.

1) Introduction:

An increasing number of clinical trials has provided compelling evidence that psychedelics, specifically psilocybin, have the potential for rapid and substantial improvement in mood disorders and substance use disorders [1-8]. These remarkable findings have ignited growing interest in elucidating the therapeutic mechanisms of psychedelics by which they operate. Psychedelics, such as psilocybin (commonly referred to as “magic mushrooms”) and lysergic dinucleotide acid (LSD) elicit profound changes in perception, mood, and cognition [9-13], collectively known as the enigmatic “psychedelic experience”. Understanding the neural basis of these effects is a crucial step towards advancing the therapeutic potential of these agents.

Recent high-profile human neuroimaging studies employing functional magnetic resonance imaging (fMRI) have shed light onto the effects of psychedelics on functional organization of neural activity [14-26]. Specifically, psychedelics have been shown to enhance brain network integration and increase global functional connectivity [15-17, 27-29]. These discoveries have led to a burgeoning body of research using fMRI to understand acute and persistent effects of psychedelics at the network level. fMRI indirectly indexes neural activity through modulations of blood-flow and metabolism that are reflected in modulations of blood oxygen level dependent (BOLD) signals. This linkage is commonly referred to as neurovascular coupling (NVC) [30-35]. For example, changes in functional connectivity are frequently interpreted as reflecting altered interregional neuronal synchrony. However, it remains uncertain whether these changes are a result of neuronal activity, alterations in vascular tone, NVC, or a combination thereof. Additionally, changes in local metabolism, respiratory rate, and head motion can also influence fMRI measures [36-51].

The hallucinogenic effects of psychedelics are dependent on activation of serotonin (5-hydroxytryptamine, 5-HT) receptors, primarily of sub-type 5-HT_{2A} (5-HT_{2A}R) [10, 27, 52-54]. The etymology of serotonin derives from its discovery as a substance in blood serum which causes vasoconstriction [55]. Serotonin was later discovered to exert neuromodulatory effects in the brain [56-59]. More recently, it was found that psychedelic 5-HT_{2A}R agonism causes dose-dependent vasoconstriction [60, 61]. Furthermore, within the central nervous system, 5-HT_{2A} receptors are expressed not only in neurons but also astrocytes [62] and other glial cells that play a pivotal role in NVC [63-67]. Considered collectively, these observations raise critical questions regarding the proper interpretation of the observed effects of psychedelics assessed by fMRI.

Genetic engineering in mice has provided new opportunities for more directly measuring neural activity [68-75]. Specifically, genetically encoded calcium indicators enable imaging of calcium activity, a key signaling molecule of synaptic activity [76-81]. In addition, optical intrinsic signal imaging can be used to measure fluctuations in oxy- and deoxy-hemoglobin concentration. Together, these techniques enable simultaneous cortex-wide measurement of neural and hemodynamic activity in mice, a modality known as wide-field optical imaging (WFOI) [69, 70, 72, 74, 82-87].

In this study, we employed WFOI in mice expressing a red-shifted genetically encoded calcium indicator in cortical Thy1+ pyramidal neurons (Thy1-jRGECO) to investigate the acute effects of psychedelic 5-HT_{2A}R agonism on neural and hemodynamic activity, functional organization, and NVC. Mice were imaged before and after injection of saline, the 5-HT_{2A}R agonist 2,5-Dimethoxy-4-iodoamphetamine (DOI), or DOI with the 5-HT_{2A}R antagonist MDL100907 (MDL) under both awake, whisker stimulation and awake, resting-state conditions. Our findings suggest that the 5-HT_{2A}R psychedelic, DOI, substantially alters NVC, warranting caution when interpreting the effects of classic psychedelic compounds on brain function assessed by hemodynamic-dependent imaging modalities.

2) Experimental methods

2.1) Mice and animal preparation

All mice were maintained in the animal facilities at Washington University in Saint Louis and all procedures were performed in strict accordance with Washington University in Saint Louis Animal Care and Use Committee requirements. Eight transgenic mice (4 males, 4 females) expressing jRGECO1a driven by the thymus cell antigen 1 (*Thy1*) promotor were used for experimentation (JAX Strain: Tg(Thy1-jRGECO1a) GP8.20Dkim/J; stock: 030525) [77, 78, 88]. Prior to imaging, a cranial window was secured to the intact skull of each mouse with dental cement under 2% isoflurane anesthesia following scalp retraction according to our previously published protocol [33] (**Fig. 1a**). One hour before surgery, mice were given buprenorphine-SR (1.0 mg/kg subcutaneous) and three days to recover before beginning handling and acclimation. Head-fixed acclimation was performed for 45 minutes a day for a week before experiments began, as previously published [72, 89-91]. All drugs were prepared on the day of experimentation. DOI (4 mg/kg), MDL (0.10 mg/kg), and saline were delivered intraperitoneally (i.p.) and, to control volumetric effects, all mice received the same total volume (20 mL/kg). After drug administration, mice were placed back in the head-fixation apparatus for 30 minutes prior to neuroimaging.

2.2) Imaging systems, data acquisition, and stimulus delivery

The experimental setup included two separate imaging systems, one for monitoring murine motion and the other for optical neuroimaging.

The motion monitoring camera (scientific complementary metal–oxide–semiconductor CMOS, Thorlabs, DCC3260C) was placed in front of the mouse. The field-of-view (FOV, ~7 cm-by-7 cm) was illuminated by a 780 nm LED (Thorlabs, M780L3, **Figs. S1a** and **S1b**). Specular reflection was minimized using crossed near-infrared polarizers (Thorlabs, LPVISC100).

For neuroimaging, a custom-built light engine with 530 nm and 625 nm LEDs provided fluorescence excitation and diffuse reflectance (**Fig. 1b**). 530 nm light (measured peak $\lambda = 525$ nm, Mightex Systems, LCS-0525-60-22) provided both fluorescent excitation and diffuse reflectance illumination, while 625nm light (measured peak $\lambda = 637$ nm, Thorlabs, M625L3) provided diffuse reflectance illumination. LED illumination was collimated using a plano-convex lens (Thorlabs, LA1433). The collimated LEDs were

placed in series using two dichroics (Mightex Systems, LCS-BC25-0605 and LCS-BC25-0560) and illumination was delivered to the exposed skull *via* a liquid light guide (Mightex Systems, LLG-05-59-420-2000-1). Diffuse reflected light from optical intrinsic signals and fluorescence emission were collected by a 75 mm focal length lens (Navitar, NMV-75M1), split by a 580 nm dichroic (Semrock, FF580-FDi02-t3-25x36) and sampled by two time-locked scientific CMOS cameras (Andor, Zyla 5.5 sCMOS). A 500 nm long pass filter (Semrock, FF01-500/LP-25) in front of Camera 1 (CMOS 1) passed 532 nm reflectance. The 580 nm dichroic and a 593 nm long pass filter (Semrock, FF01-593/LP-25) in front of camera 2 (CMOS 2) blocked 530 nm jRGECO1a excitation light and passed jRGECO1a emission and 625 nm reflectance.

A 700 nm short pass filter (Thorlabs, FESH0700) placed behind the neuroimaging camera lens blocked NIR illumination used for movement monitoring. Each neuroimaging camera sensor was cropped to 1024×1024 pixels, and 2×2 binning was performed on neuroimaging cameras to increase acquisition rate and signal-to-noise (SNR). The camera acquisition frame rate was set such that calcium and hemodynamic activity were imaged at 20 Hz. The LEDs and camera exposures were synchronized and triggered *via* a data acquisition card (National Instruments, 777643-01) using MATLAB R2021a. LED spectra were measured using an Ocean Optics USB 2000+ spectrometer.

Mice were supported by a felt pouch and mounted to the WFOI system using an aluminum bracket attached to the cranial window. The awake neuroimaging paradigm consisted of interleaved epochs of stimulus and resting-state blocks (**Fig. 1c**, top). Stimulus evoked responses were elicited through peripheral stimulation of the whiskers. Air-puff whisker stimulation was delivered to the right whiskers with a psi of 40 mmHg, a stimulus frequency of 3 Hz, and a pulse width of 100 milliseconds. Each stimulus block was 10 seconds long (*i.e.*, 30 puffs), preceded by 5 seconds of baseline imaging and followed by 15 seconds of recovery time for a total block length of 30 seconds (**Fig. 1c**, bottom). Resting-state epochs were 180 seconds long. For pre-injection imaging, task and resting-state epochs were repeated nine times, yielding a total of 31.5 minutes of imaging (*i.e.*, 27 minutes of resting-state and 4.5 minutes of task). Mice then underwent a randomized drug trial. 30 minutes after injection mice imaged according to the same procedure as the pre-injection imaging.

3) Data Analysis

3.1) Motion processing

For the movement camera, each pixel's time trace was normalized by its temporal mean to account for slight differences in scan-to-scan NIR LED illumination. Movement movies were spatially decimated by a factor of two to facilitate faster processing. For each movie, root-sum squared (RSS) traces were calculated (**Fig. S1a**) [45, 92]. For each scan, histograms of RSS time traces were calculated and averaged for each mouse. Difference histograms (post- minus pre- imaging) were calculated to determine the influence of drug on motion. For each scan, the spectral content of RSS movement traces was calculated using a smoothed power spectrum density estimate (pwelch, MATLAB 2021a). Band-limited integrated power was calculated over the infraslow band

(ISA, 0.02 - 0.08 Hz), delta band (delta, 0.5 Hz - 4.0 Hz), and the frequency range between these bands (intermediate, 0.08 Hz - 0.5 Hz).

3.2) Neuroimaging spatial normalization

Raw neuroimaging sequences (512×512 pixels) were binned off camera (4×4 binning, resulting in 128×128 pixels) to further increase the SNR of each image and to reduce the storage size of the data. Prior to neuroimaging, to address slight variations in neuroimaging camera alignment and associated FOVs, an image of a physical 10 mm by 10 mm grid was acquired by the 530 nm (CMOS1) and 625 nm (CMOS2) reflectance cameras. From these images, we identified four corresponding markers. These markers were then used to spatially coregistered the FOVs of the cameras using a projective transform. Particularly important for fluorescence imaging [93], dark frames from each camera were averaged and subtracted from that camera's image sequence. All image sequences were then affine transformed and aligned to the Paxinos atlas [94].

3.3) Neuroimaging data pre-processing

Slow trends in channel-specific light levels were temporally detrended with a 5th order polynomial fit [68, 70-73, 89-91, 95, 96]. The images were spatially smoothed using a Gaussian filter (5×5 pixel kernel, standard deviation of 1.2 pixels). Modulations in 532 nm, and 625 nm reflectance were interpreted using the modified Beer-Lambert law to calculate modulations in hemoglobin concentration: $F(\boldsymbol{r},t) = F_0 \exp\left(\Delta\mu_a(\boldsymbol{r},t)L\right)$, where $F(\boldsymbol{r},t)$ is the measured light intensity, F_0 is the baseline light intensity, $\Delta\mu_a(\boldsymbol{r},t)$ is the change from baseline in absorption coefficient due to changes in hemoglobin concentration, and L is the optical path length factor for photons traveling in tissue. L is determined analytically assuming a semi-infinite geometry [96, 97]. Changes in hemoglobin concentration were determined by inverting the system of equations: $\Delta\mu_{a,\lambda}(\mathbf{r},t) = E_{\lambda,i}\,\Delta[\mathrm{Hb}_i](\mathbf{r},t)$, where E is the extinction coefficient for hemoglobin, and i is the chromophore species (*i.e.,* oxygenated and deoxygenated hemoglobin) [96, 98-100].

Image sequences of fluorescence emission were converted to percent changes by subtracting off and dividing each pixel's time trace by its mean value ($100 \cdot (F - F_0)/F_0$). Raw collected fluorescence was corrected for hemodynamic absorption using the estimated absorption changes over the emission and excitation spectra [69]. All hemodynamic outcome measures were reported using total hemoglobin (HbT).

3.4) Signal processing

Resting-state fluctuations in calcium and hemodynamic signals were filtered to retain frequencies between 0.02 Hz - 0.08 Hz to assess infraslow activity, between 0.08 Hz – 0.5 Hz to assess intermediate frequencies, and between 0.5 Hz-4.0 Hz to assess delta band activity. Filtered signals were down sampled to 1.25 times their highest frequency. For task data and estimation of NVC (see below), data were filtered to retain frequencies between 0.01 Hz and 5 Hz and down sampled to 12 Hz. All filtering and down sampling was performed using a 5th order Butterworth filter and anti-aliasing interpolation. To minimize boundary effects, filtering was performed over the entire duration of the scan. After filtering and down sampling, resting-state and task data were

segmented into periods of rest and task using a Tukey window (Tukey parameter of 0.3) that attenuated 15% of the data at each end.

3.5) Task Analysis

To visualize the topography of the response to whisker stimulation, global signal regression was applied to increase the spatial specificity of the responses. For each pixel within the FOV, the baseline (5 seconds before stimulus onset) was subtracted from the stimulation block. Baseline corrected stimulation blocks were averaged together for each mouse and group. Maps of response amplitude were calculated for calcium (0.2-2.2 seconds following stimulus onset) and total hemoglobin (2.0-4.0 seconds following stimulus onset). Additionally, pixel-wise response effect sizes were quantified using Cohen's D, defined as

$$(\mu_{post} - \mu_{pre})/\sigma_{pooled}, \quad (1)$$

where $\mu_{pre}$and μ_{post} are the mean of the baseline and the response quantitation period, respectively, and

$$\sigma_{pooled} = \sqrt{(\sigma_{pre}^2 + \sigma_{post}^2)/2(n-1)}\ , \quad (2)$$

where σ_{pre} and σ_{post} defined as standard deviations, and *n* is the number of sample points. Spatial similarity between calcium and hemodynamic response effect maps were assessed through Pearson correlations of vectorized response effect maps.

All pre-injection effect maps (n = 24 = 8 mice·3 drug conditions) were averaged to obtain a single, high-SNR response effect map. To define a region of interest (ROI) in which all responses were quantitated, the effect map was thresholded at 75% of the maximum (**Fig. S2a**). All time traces within this ROI were averaged to evaluate stimulus evoked responses for each drug and mouse. Only evoked responses exceeding baseline (pre-stimulus) fluctuations by 2 standard deviations were included in subsequent analysis. For each mouse and condition, the average whisker stimulation response was quantified as the maximum response amplitude within the ROI. Response area was quantified as the number of pixels above 75% of this maximum response amplitude.

To assess temporal dynamics, transient and sustained responses were calculated as the integrated response between 0-5 seconds and 5-10 seconds post-stimulus onset, respectively. Effect size was calculated as Cohen's D between the pre- and post-stimulus periods.

3.6) Estimating neurovascular coupling

Neurovascular coupling (NVC) was modeled as a causal and linear shift-invariant process, $y = Xh$, where y, is the measured hemodynamic response, h is the hemodynamic response function (HRF), and X is the convolution operator, which consists of a sequence of m-shifted calcium signals. In matrix form, this equation becomes:

$$\begin{pmatrix} y_1 \\ \vdots \\ y_n \end{pmatrix} = \begin{pmatrix} x_1 & \cdots & 0 \\ \vdots & \ddots & \vdots \\ x_n & \cdots & x_{n-m} \end{pmatrix} \begin{pmatrix} h_1 \\ \vdots \\ h_m \end{pmatrix}, \tag{3}$$

where *n* is the number of sample points and *m* is the length of the convolution kernel. In this way, one can consider an output signal as a pointwise-contribution, namely h_m, to an m-shifted signal. To estimate the HRF, a weighted least squares approach was employed:

$$h = \left(X^T W X + \bar{\lambda} I\right)^{-1} X^T W, \tag{4}$$

here W is a weight matrix, $\bar{\lambda}$ is a regularization constant, and I is the identity matrix. We chose the weight matrix to be the singular value spectrum of X (*i.e.*, $X = U\mathrm{W}V^T$). The first element of W, $w_{1,1}$, is an estimate of the spectral – or operator – norm of X ($\|X\|$). To make the regularization constant appropriate for all mice and conditions, $\bar{\lambda}$ was defined as $\bar{\lambda} = \lambda \cdot \|X^T W X\|$, where the fractional regularization constant, λ, was empirically set to $\lambda = 10^{-5}$ (see footnote[1]).

Prior to calculation, an artificial 3 second delay was introduced between x and y to allow for examination of the temporal relation prior to time zero. To assess the frequency-dependent properties of calcium-to-hemodynamic transduction dynamics, transfer functions (TF) were defined as the power spectral density estimate of the impulse response function, h.

Regional NVC was quantified by averaging all time courses within anatomical regions defined in the Paxinos atlas [94]. The resulting regional time courses were segmented into 30 second, non-overlapping, windows (Tukey window, lobe parameter of 0.3). HRFs were estimated for each 30 second epoch and the median across all epochs defined a regional HRF. Regional estimated HRFs were averaged across regions to obtain a cortical-wide (global) estimate of NVC. Temporal properties of all regional and global HRFs were evaluated by calculating the peak value (peak), time to peak (TTP), and full width at half maximum (FWHM). The frequency dependent properties of each HRF were evaluated as bandlimited power over the ISA, intermediate, and delta bands. Lastly, measured calcium activity was convolved with the HRF to produce predicted hemodynamic signals. Pearson's correlation between predicted hemodynamic signals and measured hemodynamic signals was calculated to assess model fit.

---

[1] We note here that, for non-symmetric matrices, there is no straight-forward way to estimate the spectral norm of a product of matrices through the spectral norms of the constituents. But we note that the sub multiplicative property of spectral norm states that $\|AB\| \leq \|A\| \cdot \|B\|$, so that $\|ABC\| \leq \|AB\| \cdot \|C\| \leq \|A\| \cdot \|B\| \cdot \|C\|$. We also note that $\|X\|$=$\|X^T\| = \|W\| = w_{1,1}$. Therefore $\|X^T W X\| \leq w_{1,1}^3$

3.7) Quantification of resting-state activity

Power spectral density estimates (PSD) of resting-state activity was calculated using a smooth spectral estimator (pwelch, MATLAB2022). For each region in the Paxinos atlas, PSDs were averaged over the 9 resting-state epochs. Regional spectra were integrated over ISA, intermediate, and delta bands. Global PSDs for each mouse were calculated by averaging PSDs across all cortical regions. Mouse-level PSDs were averaged to obtain group-level cortical resting-state PSDs.

3.8) Resting-state functional connectivity

Measures of resting-state functional connectivity (RSFC) were calculated using zero lag correlation for all pixel pairs within our field of view, as in previous reports [68, 70, 89, 91, 96]. Briefly, spontaneous activity was filtered over infraslow and delta bands. Global signal regression was performed to increase the spatial specificity of the RSFC maps [42-44]. Pairwise correlation matrices were reordered according to Paxinos atlas regions. Region-based RSFC maps were computed by averaging across rows of the reordered matrices. RSFC maps of frontal, cingulate, retrosplenial, and secondary motor (M2) cortices were reported.

To contrast changes in calcium-based and hemodynamic-based RSFC arising from different pharmacological agents, RSFC post minus pre difference matrices were computed. Spatial similarity (correlation) and linear relations (linear regression) were assessed for these RSFC difference matrices. Specifically, matrix correlations were evaluated as Pearson correlations between vectorized difference RSFC matrices. Linear regressions were evaluated as:

$$y = \beta_1 x + \beta_0, \tag{5}$$

where x and y are vectorized RSFC difference maps for calcium and HbT, respectively.

3.9) Statistics

For movement RSS traces and band-limited spectral content, significance of drug effect was determined using a Kruskal-Wallis one-way analysis of variance. For stimulus-evoked responses and associated HRFs and TFs, results are reported as medians and percentiles. Parameters extracted from HRFs, and TFs were calculated as percent changes from pre-injection. Significance of drug effects was determined using a Kruskal-Wallis one-way analysis of variance. Post-hoc significance was assessed using the paired Wilcoxon sign-rank test. Multiple comparisons were corrected using the Bonferroni correction. Significant of the effect of time (*i.e.*, pre-, and post- injection comparisons) was assessed using the paired Wilcoxon signed-rank test.

PSDs were compared across drugs through integrated double octave bins. Effects of drugs were determined through one-way analysis of variance (ANOVA) and post-hoc paired t-tests. The effect of time (*i.e.*, pre- versus post- injection) was determined to be significant using paired t-tests and corrected for multiple corrections using Bonferroni correction.

For all RSFC measures, Pearson r correlation coefficients were converted to Fisher z values prior to any mathematical operation and reverted to Pearson correlations for reporting. For seed based RSFC maps, clustering statistics were employed [101, 102], with a clustering threshold of 3 contiguous pixels.

4) Results

4.1) DOI does not induce movement during WFOI head restraint

To evaluate the impact of DOI on adventitious motion [45, 46, 48, 92, 103-105] and the well-established head-twitch responses to $5HT_{2a}$ receptor agonism [106-109], we calculated the RSS of movement movies both before and after administrating of drugs. Pre- versus post- injection RSS histograms were not significantly different for any drug. Furthermore, movement difference distributions (*i.e.*, post- minus pre- injection) were not significantly different across different drugs (**Fig. S1b**). Spectral estimates did not differ over time (pre- versus post-injections), drug condition, or frequency band (**Fig. S1c**).

4.2) DOI alters stimulus response dynamics, response topography, and neurovascular coupling

4.2.1) Peripheral whisker response dynamics and topography

Whisker stimulation induced focal calcium and hemodynamic responses on primary somatosensory barrel cortex and distant portions of secondary motor cortex (**Fig. 2a**). Auditory responses were observed and attributable to air puff sounds. Administration of DOI modulated response dynamics and topography. Moreover, DOI elicited discrepancies in calcium versus hemodynamic response topography; specifically, a reduced calcium response in retrosplenial and posterior cingulate regions, but a decreased hemodynamic response in the somatomotor region and an increased hemodynamic response in contralateral auditory cortex (black arrows in **Fig. 2a**). This change in topography was quantified in terms of spatial correlation. DOI decreased spatial correlations between calcium and hemodynamic responses.

Differences between calcium (**Fig. S2b**, top) versus hemodynamic responses within the ROI were observed (**Fig. S2b**, bottom). Specifically, DOI induced a decreased calcium response effect. In contrast, stimulus-evoked hemodynamic response effects showed no significant effect of time (*i.e.*, post- versus pre-injection) or drug.

Next, to investigate the temporal dynamics of calcium and hemodynamic stimulus responses, we averaged time traces of all pixels within the ROI to yield high-SNR signals (**Fig. 2b**). We evaluated and compared peak response magnitude and the transient (0-5 seconds after stimulation onset) and sustained components (5-10 seconds after stimulation onset). DOI increased both calcium and calcium sustained responses. In contrast, hemodynamic sustained responses decreased after both DOI and DOI+MDL responses. Interestingly, we also found that DOI decreased the hemodynamic response effect, but not the calcium response effect. Considered collectively, these results suggest a differential impact of DOI on calcium versus hemodynamic responses to peripheral whisker stimulation.

4.2.2) Stimulus-response neurovascular coupling

In view of contrasting neuronal and hemodynamic whisker stimulation responses under DOI conditions, we determined the impact of DOI on neurovascular coupling. NVC was modelled (See 3.6) and the data were fit to yield estimates of HRFs (**Fig. 3a**). Prior to administration of any drug (**Fig. 3a**, reds), the HRFs closely matched previously published results [69]. After administration of DOI, the FWHM of the HRF decreased (**Fig. S2c**).

Narrowing of the HRF implied that DOI emphasized high frequencies in the responses. As anticipated, DOI increased transduction in frequencies above 0.5 Hz (**Fig. 3b**). Importantly, this effect reversed when DOI was administered with MDL.

4.3) Calcium and hemodynamic resting-state power exhibit distinct features under DOI

Several observations spanning human and animal models indicate that psychedelics markedly alter resting-state hemodynamic activity [14, 25, 26, 110] and neuronal synchronization [111-115]. To complement these studies, we characterized changes in resting-state power arising from 5-HT_{2A}R agonism through DOI administration.

4.3.1) Global resting-state activity power

Before drug administration, global resting-state calcium signals exhibited one-over-f like spectra (**Fig. 4a**), in accordance with previous studies [68, 73, 96, 116]. Following saline, calcium power decreased above 0.08 Hz (**Fig. S3a**). After DOI, calcium power exhibited a similar trend in decreased power between 0.08 Hz and 0.64 Hz, but also consistently exhibited increased power above 0.32 Hz. In contrast to saline and DOI, DOI+MDL largely preserved pre-injection power spectral characteristics.

Global resting-state hemodynamic activity revealed a different picture. Before drug administration, hemodynamics also exhibited one-over-f like spectra, but with a steeper falloff (**Fig. 4b**). As observed with calcium, DOI gave rise to increased power in lower-delta band frequencies (**Fig. S3b**), however, this effect peak was broader and shifted to lower frequencies. Following injection of DOI+MDL, spectra returned to their pre-injection characteristics.

4.3.2) Regional resting-state activity power

We next examined regional specificity of global alterations in cortical power spectra (**Figs. 4c** and **S4**). Regional spectra were integrated over standard functional bands (ISA, intermediate, and delta, **Fig. S4**). Following saline administration, calcium integrated power was relatively unchanged across all functional bands (**Fig. S4a**). DOI induced multiple changes in power spectrum characteristics which strongly differed between calcium and hemodynamic signals (**Fig. 4c**). In particular, a hemodynamic delta band peak (**Fig. 4c**, right) emerged in all regions excluding cingulate and retrosplenial cortex. A similar, but weaker, effect was evident in the calcium signal (**Fig. 4c**, left), shifted to higher frequencies. Interestingly, in contrast to observations in hemodynamic signals, retrosplenial and cingulate cortex were not distinguished from other parts of the cortex in the calcium signals. In the intermediate frequencies, calcium

activity decreased in all cortical regions excluding frontal and cingulate. In contrast, hemodynamic signals decreased in frontal and cingulate cortex. Lastly, DOI gave rise to increased calcium ISA power in frontal, cingulate, and motor cortices while hemodynamic ISA activity increased primarily in somatosensory regions. Notably, DOI largely increased hemodynamic activity in the somatosensory Hindpaw region (see Supplemental 2.1). As observed in Figures 2 and 3, MDL largely reversed the effects of DOI. The topography of these effects is illustrated in **Fig. S4**.

Considered collectively, our results thus far reveal that, at both local and global scales, DOI induced distinct alterations in cortical excitatory fluctuations compared to hemodynamic fluctuations. Notably, these effects were attenuated when DOI was combined with MDL, indicating a mechanism that relies on the activation of the $5HT_{2A}$ receptor.

4.4) DOI alters resting-state neurovascular coupling

Following the observation of differential changes in resting-state calcium and hemodynamic activity, we next investigated causal relations between calcium and hemodynamic signals. To that end, HRFs and TFs were evaluated globally (**Figs. 5a-b** and **S3c**) and regionally (**Figs. 5c** and **S5**).

4.4.1) Global resting-state neurovascular coupling

Prior to administration of any drug, resting-state canonical HRFs [69] closely resembled pre-injection stimulus-response HRFs (**Fig. 5a**). Following DOI, the HRF deviated from the canonical form. Specifically, the HRFs exhibited a peak before time zero; this feature suggests an acausal component (see Discussion 5.3.1) and was also observed in lagged cross covariance analysis (**Figs. S6** and **S7**, Supplemental 2.3). Moreover, DOI gave rise to increased TTP, reduced model fit, and decreased FWHM. Additionally, DOI induced a quasi-oscillatory feature in the lower delta band, evident in the TF (**Fig. 5b and Fig. S3c**).

4.4.2) Regional resting-state neurovascular coupling

Recent work has highlighted that NVC, even in healthy subjects, varies over the cortex [117-121]. Following our observations of drug-and-region-specific differences in calcium and hemodynamic power, we next investigated whether the effects of $5\text{-}HT_{2A}R$ agonism differentially affect regional NVC [122]. HRFs and TFs were calculated regionally (**Fig. S5**, Supplemental 2.2), parameterized, and visualized on the cortex (**Fig. 5c**). As observed before in other measures, DOI differentially altered HRFs and TFs across the cortex.

DOI induced focal, reversible NVC effects (peak value, TTP, FWHM, and delta band transduction) of opposite polarity in higher order association regions (*e.g.*, frontal, and cingulate) versus lateral somatosensory and parietal regions (**Fig. 5c**). Large decreases in strength of coupling (reflected in lower peak values in the HRF) were observed in frontal/cingulate regions while the more modest increases occurred in whisker-barrel cortex. DOI increased a NVC delay (reflected by increased TTP) in frontal and anterior-lateral parts of somatomotor cortex.

The most striking changes in NVC were observed in terms of FWHM and, closely related, delta band transduction. DOI significantly reduced FWHM across the entire cortex with the most substantial decreases occurring in cingulate and frontal regions. DOI massively increased delta band transduction in almost all cortical regions, except for cingulate regions, which exhibited a decrease. Notably, delta transduction was substantially increased in the somatosensory whisker-barrel cortex.

4.5) DOI modifies functional organization

Several observations spanning humans and animals indicate that psychedelics markedly alter resting-state hemodynamic activity [14, 25, 26, 110] and neuronal synchronization [111-115, 123]. To complement these reports, we characterized the effects of DOI on calcium versus hemodynamic measures of cortical RSFC at the global and local scales.

4.5.1) Calcium and hemodynamic measures of RSFC: ISA band

Human fMRI has revealed profound alterations in brain organization following psychedelic agent administration, particular in brain regions associated with higher order cognitive processes [15-17, 27-29]. However, it remains unclear if these observations represent alterations in neuronal activity, NVC, or some combination thereof.

We investigated RSFC in the ISA band using seeds in frontal, cingulate, retrosplenial, and secondary motor regions (**Fig. 6**). Before injection (**Fig. 6a-d**, top), both calcium and hemodynamic RSFC maps exhibited network topographies consistent with extensive prior results [70, 72, 73, 89, 95, 96]. Briefly, these topographies were characterized by strong intra-network connectivity (reflected by high correlations) and network-specific anticorrelations (*i.e.*, primarily along the anterior-posterior axis for the frontal, retrosplenial, and M2 regions, and along the medial-lateral axis for the cingulate regions). Saline administration had no impact on calcium or hemodynamic RSFC.

DOI administration profoundly altered cortical-wide RSFC. Specifically, DOI enhanced intra-network calcium functional connectivity within the cingulate region (**Fig. 6b**) and inter-network calcium connectivity between cingulate and frontal regions (**Fig. 6a-b**). Moreover, DOI profoundly altered retrosplenial calcium functional connectivity across the cortex as follows: (1) enhanced negative connectivity between the cingulate and posterior-lateral parts of retrosplenial regions (**Fig. 6b**) and (2) strengthened connectivity between cingulate/frontal and anterior-medial parts of retrosplenial regions (**Fig. 6a-b**). Furthermore, DOI significantly reduced connectivity between the retrosplenial cortex and portions of the visual network (**Fig. 6c**). MDL markedly attenuated most calcium RSFC changes induced by DOI. However, retrosplenial connectivity remained perturbed in frontal, parts of anterior sensorimotor, and visual regions (**Fig. 6c**).

Strikingly, almost none of the RSFC changes measured through calcium signals were observed in blood-based measures of RSFC. For example, DOI induced small

increases in inter-network hemodynamic functional connectivity between frontal and retrosplenial regions. Additionally, connectivity between retrosplenial and anterior cingulate regions increased. As observed with calcium based RSFC, MDL reversed most of the RSFC changes induced by DOI.

In many cases, hemodynamic and calcium RSFC changes exhibited markedly different topographies. Spatial correlation and regression between RSFC maps were employed to quantify the disparities between calcium- and hemodynamic-based RSFC measures. Regression of RSFC changes (**Fig 6**) measured through calcium and hemodynamics was calculated (**Table 1**). Where the calcium and hemodynamic functional connectivity both were present, DOI consistently decreased the correlation and proportionality (*i.e.*, β, refer to Eq. 5) of the linear relation between the two measures. Most of these discrepancies between calcium and hemodynamics were reversed by MDL. The addition of MDL to DOI produced anomalous RSFC effects as assessed with the cingulate seed. These results suggest that, before administration of drugs, RSFC evaluated through calcium and hemodynamic signals are, in many cases, topographically similar, although quantitatively different. However, DOI induces substantial disparities between calcium versus hemodynamics RSFC.

4.5.1) Calcium measures of RSFC: Delta band

Another advantage of calcium-based measures of RSFC is access to faster signaling not reflected in cortical hemodynamics. As previously reported, resting-state delta band fluctuations (0.5 Hz- 4.0 Hz) reveals distinct RSFC topography compared to ISA, even in the absence of drugs [70, 72, 73] (**Fig. 6a-d**, right). Saline did not alter RSFC in any region, excluding minimal increases in functional connectivity between cingulate and retrosplenial regions.

In contrast, DOI modified cortical-wide inter- and intra -network connectivity. The most prominent feature of DOI-induced modifications in RSFC was the wide-spread decrease in retrosplenial connectivity with the rest of the cortex; retrosplenial connectivity decreased the most in cingulate and frontal regions (**Fig. 6a-d**). Moreover, large increases in connectivity arose between frontal and medial motor/anterior lateral somatosensory regions (**Fig. 6a**) and cingulate and parietal, and cingulate and frontal regions (**Fig. 6a**). Interestingly, the effect of DOI as assessed with frontal and retrosplenial seeds was topographically similar, but of opposite sign (**Fig. 6c** compared to **Fig. 6b**). Co-administration of DOI and MDL largely reversed the effects of DOI.

5.) Discussion

5.1) Summary of present findings

We conducted WFOI to assess the effects of the psychedelic, DOI, on cortical neuronal and hemodynamic responses to whisker stimulation and spontaneous activity in the resting-state. Simultaneous imaging of calcium and hemodynamic signals enabled assessment of NVC, both in the time domain (*i.e.*, HRFs) and the frequency domain (*i.e.*, TFs). Under both task and resting-state conditions, DOI narrowed HRFs and enhanced transduction of higher frequency neuronal activity, especially in the delta

band. Additionally, DOI introduced a zero-lag notch in the resting-state HRF, a phenomenon absent in DOI task-based HRFs (see section 5.3.1).

These DOI-induced alterations in NVC were regionally specific and especially prominent in association regions, parts of the cortex expressing high densities of 5-HT_{2A} receptors [62, 124-127]. Co-administration of DOI and MDL largely reversed the effects of DOI on NVC. DOI-induced alterations in NVC imply a dissociation between neuronal versus hemodynamic signals. For example, in our results, DOI substantially decoupled calcium versus hemodynamic RSFC (**Fig. 6**) and signal power (**Figs. 4**, **S4**, and **S4**). Such dissociations carry widespread implications regarding the interpretation of purely hemodynamic measures of brain function such as human BOLD-fMRI.

5.2) Prior research

5.2.1) Neuronal signatures of psychedelic intoxication

Classic psychedelics are 5-HT_{2A} receptor agonists [10, 26, 27, 52-54, 128-130]. This receptor subtype is predominantly located in cortical regions associated with "higher" cognitive functions (*e.g.*, prefrontal, and anterior cingulate cortex) [62, 124-127]. These regions are thought to be key mediators of the psychedelic experience [53, 61, 103, 123-127, 131, 132]. Invasive electrophysiological studies have demonstrated regionally specific modulations of neuronal excitability following psychedelic administration [111-113, 115, 133-136]. For instance, administration of DOI increased pyramidal neuronal firing rate and decreased LFP low-frequency power in rat prefrontal cortex. These effects were only partially reversed by MDL, potentially reflecting DOI affinity for other receptors such as 5-HT_{2C} receptors [111, 123]. Although these studies are informative, they reflect regional expression of receptor subtypes [133, 137-139] and may not capture brain-wide emergent phenomenology [140], as does fMRI and WFOI.

5.2.2) Effects of psychedelic agents on resting-state fMRI in humans

Recent resting-state fMRI studies in humans have indirectly assessed the effects of psychedelic agents with brain-wide coverage [14-25]. Notwithstanding some preprocessing-dependent inconsistencies [139, 141], the consensus is that psilocybin reduces functional connectivity within association networks, particularly within the default mode network [14, 23-25, 142]. This effect has been hypothesized to reflect the subjective experience of ego dissolution [11, 16, 27, 29]. Additionally, many studies have reported increased functional connectivity between association networks and other parts of the brain [16, 19, 29, 115, 135, 139, 140]. Psychedelics induce dissolution and fragmentation of canonical RSFC patterns that were quantitated using entropic measures [11, 17, 19, 140]. These studies all imply that psychedelics modulate neural activity throughout the brain. However, the interpretation of purely hemodynamic measures is incomplete without consideration of the neurovascular effects of psychedelics.

5.2.3) Neurovascular coupling

Apart from neuromodulation [122, 143-147], serotonin has potent vasoactive effects [60, 61, 148]. For example, serotonin binding triggers vasoconstriction through intracellular signaling pathways involving phospholipase C, calcium release, and protein kinase C

phosphorylation [149]. Moreover, serotonin can directly modulate blood flow by activating serotonin receptors on blood vessels [148]. Further, 5-HT_{2A} receptors are expressed on astrocytes [62], cells that play a crucial role in NVC [63-67, 150-152].

Serotonin can also less directly regulate NVC *via* the close association between serotonergic neurons, microvessels, and perivascular astrocytes [148, 153, 154]. These effects include changes in systemic physiology (*e.g.,* respiratory rate, cardiac rate, blood pressure) that influence neurovascular relations [48, 50, 118, 155-159]. Prior psychedelic research has demonstrated prominent effects on systemic physiology [27, 160], further suggesting that psychedelic agents potentially modulate NVC.

5.3) DOI disrupts neurovascular coupling

DOI focally increased calcium activity in the delta band (**Figs. 4** and **S4**). This observation is concordant with prior EEG studies in humans on the effects of psychedelics other than DOI [113, 114, 161, 162]. In the present data, increased delta band activity was observed in hemodynamic signals (**Figs. 4** and **S4**), as reflected in increased delta band NVC (**Figs. 5** and **S5**). Enhanced delta-band NVC was differentially prominent in lateral portions of the mouse cortex (**Fig. 5c**, bottom). This topography potentially corresponds to a main effect of psychedelics in humans, specifically, loss of functional segregation between primary cortical regions (*e.g.*, somatosensory, and visual) and the default mode network assessed in the infraslow band (*i.e.*, frequencies below 0.1 Hz) [24, 25, 28, 142, 163, 164].

5.3.1) A potential retrograde calcium-to-hemodynamic relation

DOI induced a zero-lag notch in the lagged cross-covariance (CCF, **Fig. S6a**, Supplemental 2.3) and hemodynamic response functions (HRF, **Fig. 5a**), which could represent a retrograde relation (*i.e.*, a negative lag peak). Importantly, the prominence of this phenomenon was regionally dependent (*e.g.*, largest in secondary motor and retrosplenial regions, **Figs. S7a** and **S5a**). This phenomenon appears in the frequency domain as a broad peak around ~0.8 Hz (**Figs. 5b** and **S6b**) that exhibited focal features (largest in retrosplenial, secondary motor, and cingulate regions **Figs. S5b** and **S7b**).

A constant slope in the phase plot indicates a fixed temporal lag [165]. On average, before drugs, the calcium-to-hemodynamic phase relation exhibited a positive slope at frequencies between zero and ~1 Hz (**Fig. S6c**), indicating that calcium leads hemodynamics in this band. However, DOI and DOI+MDL induced negative phase slopes in specific cortical regions within the same frequency band (frontal, and cingulate regions **Fig. S7c**). This result suggests that hemodynamics leads calcium in these areas, a remarkable difference from the pre-drug state.

This feature could potentially arise from DOI-induced alterations in (1) the calcium-hemodynamic relation (a neurobiological account) or (2) misinterpretation of the optical data (artifact). In the artifactual account, the notch may represent the superposition of a high-frequency anticorrelation on a temporally broad (low frequency) lag-dependent relation. However, importantly, we note that this phenomenon is not present in

responses to stimuli (**Fig. 3a**), which were subjected to the same data analysis. Further, the notch was unequally present over the cortex, which argues against artifact.

An alternative account of this feature is DOI-dependent neurobiology. In this framework, the zero-lag notch arises from the superposition of two neurobiological phenomena: neuro-vascular coupling and vasculo-neural coupling [117, 159, 166-168]. For instance, inadequate blood flow, which may result in variations in oxygen and nutrient delivery to neurons, has the potential to disrupt firing patterns [166, 169]. According to this perspective, psilocybin administration increases metabolic demand across the neocortex [170]. If this demand is not met through sufficient blood flow, neuronal activity can be modulated, giving rise to a potentially important retrograde relation.

5.4) Limitations

Although our NVC model accounts for many features of the observed data, it assumes causality, linearity, and time-invariance. These assumptions may oversimplify NVC. The most salient example of this oversimplification is the HRF measured after DOI, which contains a primary (positive lag) and secondary (negative lag) peak. Therefore, more comprehensive models of coupling between neuronal (calcium) and hemodynamic activity could consider the addition of nonlinear, “retrograde” steps or could address self-modulation, mutual information, cross-frequency coupling, or recursion of the input signals [171-174].

Additionally, several observations under DOI conditions were not fully reversed by the 5-HT_{2A}R antagonist, MDL, which raises the question of receptor-dependent psychedelic effects outside of 5-HT_{2A}R binding [175-179]. Investigating a broader range of compounds [180-182] and receptor subtypes could provide a more comprehensive understanding of the physiology underlying psychedelic effects.

Our findings raise questions that can only be addressed with more direct measures of neuronal activity and NVC. In human studies, this could be achieved with simultaneous EEG-fMRI [183-185] with consideration of NVC. Wide field optical imaging is sensitive to hemodynamic activity in frequencies extending up to ~5 Hz (**Fig. 4b**). The most significant present hemodynamic effect of DOI occurred at frequencies above 0.2 Hz. The extent to which this phenomenon is relevant to human fMRI studies is uncertain as BOLD-fMRI signals are markedly attenuated at frequencies above ~0.2 Hz in awake humans [186, 187]. To address this limitation, optical techniques such as diffuse optical tomography could be employed to measure cortical hemodynamics with high spatiotemporal resolution [188, 189].

More broadly, psychedelic research could benefit from a more cautious stance towards the conventional neurocentric BOLD-fMRI model [190]. This shift encourages a broader, more holistic perspective concerning the genesis of blood-based signals [48, 50, 63-67, 150-152, 155, 159, 191-194]. Such an approach could improve our understanding of the effects of psychedelics on brain function and NVC.

References:

1. von Rotz, R., et al., *Single-dose psilocybin-assisted therapy in major depressive disorder: A placebo-controlled, double-blind, randomised clinical trial.* EClinicalMedicine, 2023. **56**: p. 101809.
2. Jensen, M.E., et al., *Psilocybin-assisted therapy for reducing alcohol intake in patients with alcohol use disorder: protocol for a randomised, double-blinded, placebo-controlled 12-week clinical trial (The QUANTUM Trip Trial).* BMJ Open, 2022. **12**(10): p. e066019.
3. Davis, A.K., et al., *Effects of Psilocybin-Assisted Therapy on Major Depressive Disorder: A Randomized Clinical Trial.* JAMA Psychiatry, 2021. **78**(5): p. 481-489.
4. Bogenschutz, M.P., et al., *Percentage of Heavy Drinking Days Following Psilocybin-Assisted Psychotherapy vs Placebo in the Treatment of Adult Patients With Alcohol Use Disorder: A Randomized Clinical Trial.* JAMA Psychiatry, 2022. **79**(10): p. 953-962.
5. Bogenschutz, M.P., et al., *Clinical Interpretations of Patient Experience in a Trial of Psilocybin-Assisted Psychotherapy for Alcohol Use Disorder.* Front Pharmacol, 2018. **9**: p. 100.
6. Thomas, K., B. Malcolm, and D. Lastra, *Psilocybin-Assisted Therapy: A Review of a Novel Treatment for Psychiatric Disorders.* J Psychoactive Drugs, 2017. **49**(5): p. 446-455.
7. Madras, B.K., *Psilocybin in Treatment-Resistant Depression.* N Engl J Med, 2022. **387**(18): p. 1708-1709.
8. Raison, C.L., et al., *Single-Dose Psilocybin Treatment for Major Depressive Disorder: A Randomized Clinical Trial.* JAMA, 2023. **330**(9): p. 843-853.
9. Watts, R., et al., *Patients' accounts of increased "connectedness" and "acceptance" after psilocybin for treatment-resistant depression.* Journal of humanistic psychology, 2017. **57**(5): p. 520-564.
10. Vollenweider, F.X. and M. Kometer, *The neurobiology of psychedelic drugs: implications for the treatment of mood disorders.* Nat Rev Neurosci, 2010. **11**(9): p. 642-51.
11. Lebedev, A.V., et al., *LSD-induced entropic brain activity predicts subsequent personality change.* Hum Brain Mapp, 2016. **37**(9): p. 3203-13.
12. Griffiths, R.R., et al., *Psilocybin occasioned mystical-type experiences: immediate and persisting dose-related effects.* Psychopharmacology (Berl), 2011. **218**(4): p. 649-65.
13. Carhart-Harris, R.L., et al., *LSD enhances suggestibility in healthy volunteers.* Psychopharmacology (Berl), 2015. **232**(4): p. 785-94.
14. Carhart-Harris, R.L., et al., *Neural correlates of the psychedelic state as determined by fMRI studies with psilocybin.* Proceedings of the National Academy of Sciences, 2012. **109**(6): p. 2138-2143.
15. Roseman, L., et al., *The effects of psilocybin and MDMA on between-network resting state functional connectivity in healthy volunteers.* Front Hum Neurosci, 2014. **8**: p. 204.
16. Lebedev, A.V., et al., *Finding the self by losing the self: Neural correlates of ego-dissolution under psilocybin.* Hum Brain Mapp, 2015. **36**(8): p. 3137-53.
17. Carhart-Harris, R.L., et al., *The entropic brain: a theory of conscious states informed by neuroimaging research with psychedelic drugs.* Front Hum Neurosci, 2014. **8**: p. 20.
18. Atasoy, S., et al., *Common neural signatures of psychedelics: Frequency-specific energy changes and repertoire expansion revealed using connectome-harmonic decomposition.* Prog Brain Res, 2018. **242**: p. 97-120.

19. Viol, A., et al., *Shannon entropy of brain functional complex networks under the influence of the psychedelic Ayahuasca.* Sci Rep, 2017. **7**(1): p. 7388.
20. Deco, G., et al., *Whole-Brain Multimodal Neuroimaging Model Using Serotonin Receptor Maps Explains Non-linear Functional Effects of LSD.* Curr Biol, 2018. **28**(19): p. 3065-3074 e6.
21. Petri, G., et al., *Homological scaffolds of brain functional networks.* J R Soc Interface, 2014. **11**(101): p. 20140873.
22. Atasoy, S., et al., *Critical brain dynamics under LSD revealed by connectome-specific harmonic decomposition.* Scientific Reports, 2017. **7**: p. 17661.
23. Carhart-Harris, R.L., et al., *Implications for psychedelic-assisted psychotherapy: functional magnetic resonance imaging study with psilocybin.* Br J Psychiatry, 2012. **200**(3): p. 238-44.
24. Palhano-Fontes, F., et al., *The psychedelic state induced by ayahuasca modulates the activity and connectivity of the default mode network.* PLoS One, 2015. **10**(2): p. e0118143.
25. Tagliazucchi, E., et al., *Enhanced repertoire of brain dynamical states during the psychedelic experience.* Hum Brain Mapp, 2014. **35**(11): p. 5442-56.
26. Carhart-Harris, R.L., et al., *The paradoxical psychological effects of lysergic acid diethylamide (LSD).* Psychol Med, 2016. **46**(7): p. 1379-90.
27. Carhart-Harris, R.L., et al., *Neural correlates of the LSD experience revealed by multimodal neuroimaging.* Proc Natl Acad Sci U S A, 2016. **113**(17): p. 4853-8.
28. Muller, F., et al., *Altered network hub connectivity after acute LSD administration.* Neuroimage Clin, 2018. **18**: p. 694-701.
29. Tagliazucchi, E., et al., *Increased Global Functional Connectivity Correlates with LSD-Induced Ego Dissolution.* Curr Biol, 2016. **26**(8): p. 1043-50.
30. Heeger, D.J. and D. Ress, *What does fMRI tell us about neuronal activity?* Nature reviews neuroscience, 2002. **3**(2): p. 142-151.
31. Hyder, F., et al., *Quantitative functional imaging of the brain: towards mapping neuronal activity by BOLD fMRI.* NMR in Biomedicine: An International Journal Devoted to the Development and Application of Magnetic Resonance In Vivo, 2001. **14**(7-8): p. 413-431.
32. Drew, P.J., *Vascular and neural basis of the BOLD signal.* Current opinion in neurobiology, 2019. **58**: p. 61-69.
33. Kim, D.-S., et al., *Spatial relationship between neuronal activity and BOLD functional MRI.* Neuroimage, 2004. **21**(3): p. 876-885.
34. Heeger, D.J., et al., *Spikes versus BOLD: what does neuroimaging tell us about neuronal activity?* Nature neuroscience, 2000. **3**(7): p. 631-633.
35. Sotero, R.C. and N.J. Trujillo-Barreto, *Modelling the role of excitatory and inhibitory neuronal activity in the generation of the BOLD signal.* Neuroimage, 2007. **35**(1): p. 149-65.
36. Shmuel, A. and D.A. Leopold, *Neuronal correlates of spontaneous fluctuations in fMRI signals in monkey visual cortex: Implications for functional connectivity at rest.* Human brain mapping, 2008. **29**(7): p. 751-761.
37. Gusnard, D.A., M.E. Raichle, and M.E. Raichle, *Searching for a baseline: functional imaging and the resting human brain.* Nat Rev Neurosci, 2001. **2**(10): p. 685-94.

38. Buxton, R.B., *Dynamic models of BOLD contrast.* Neuroimage, 2012. **62**(2): p. 953-61.
39. Logothetis, N.K., *What we can do and what we cannot do with fMRI.* Nature, 2008. **453**(7197): p. 869-878.
40. Liu, T.T., *Neurovascular factors in resting-state functional MRI.* Neuroimage, 2013. **80**: p. 339-48.
41. Ances, B.M., et al., *Effects of aging on cerebral blood flow, oxygen metabolism, and blood oxygenation level dependent responses to visual stimulation.* Hum Brain Mapp, 2009. **30**(4): p. 1120-32.
42. Murphy, K. and M.D. Fox, *Towards a consensus regarding global signal regression for resting state functional connectivity MRI.* Neuroimage, 2017. **154**: p. 169-173.
43. Fox, M.D., et al., *The global signal and observed anticorrelated resting state brain networks.* J Neurophysiol, 2009. **101**(6): p. 3270-83.
44. Murphy, K., et al., *The impact of global signal regression on resting state correlations: are anti-correlated networks introduced?* Neuroimage, 2009. **44**(3): p. 893-905.
45. Power, J.D., et al., *Spurious but systematic correlations in functional connectivity MRI networks arise from subject motion.* Neuroimage, 2012. **59**(3): p. 2142-54.
46. Power, J.D., B.L. Schlaggar, and S.E. Petersen, *Recent progress and outstanding issues in motion correction in resting state fMRI.* Neuroimage, 2015. **105**: p. 536-51.
47. Birn, R.M., K. Murphy, and P.A. Bandettini, *The effect of respiration variations on independent component analysis results of resting state functional connectivity.* Hum Brain Mapp, 2008. **29**(7): p. 740-50.
48. Jones, T.B., P.A. Bandettini, and R.M. Birn, *Integration of motion correction and physiological noise regression in fMRI.* Neuroimage, 2008. **42**(2): p. 582-590.
49. Birn, R.M., et al., *fMRI in the presence of task-correlated breathing variations.* Neuroimage, 2009. **47**(3): p. 1092-104.
50. Birn, R.M., *The role of physiological noise in resting-state functional connectivity.* Neuroimage, 2012. **62**(2): p. 864-70.
51. Kennan, R.P., et al., *Physiological basis for BOLD MR signal changes due to neuronal stimulation: separation of blood volume and magnetic susceptibility effects.* Magn Reson Med, 1998. **40**(6): p. 840-6.
52. Carhart-Harris, R.L., *Serotonin, psychedelics and psychiatry.* World Psychiatry, 2018. **17**(3): p. 358-359.
53. Vargas, M.V., et al., *Psychedelics promote neuroplasticity through the activation of intracellular 5-HT2A receptors.* Science, 2023. **379**(6633): p. 700-706.
54. Kelmendi, B., et al., *Psychedelics.* Curr Biol, 2022. **32**(2): p. R63-R67.
55. Rapport, M.M., A.A. Green, and I.H. Page, *Serum vasoconstrictor, serotonin; isolation and characterization.* J Biol Chem, 1948. **176**(3): p. 1243-51.
56. Gaddum, J.H. and Z.P. Picarelli, *Two kinds of tryptamine receptor.* Br J Pharmacol Chemother, 1957. **12**(3): p. 323-8.
57. Page, I.H., *Serotonin (5-hydroxytryptamine); the last four years.* Physiol Rev, 1958. **38**(2): p. 277-335.
58. Iversen, L.L., *Role of transmitter uptake mechanisms in synaptic neurotransmission.* Br J Pharmacol, 1971. **41**(4): p. 571-91.

59. Carlsson, A., *The occurrence, distribution and physiological role of catecholamines in the nervous system.* Pharmacol Rev, 1959. **11**(2, Part 2): p. 490-3.
60. Dyer, D.C. and D.W. Gant, *Vasoconstriction produced by hallucinogens on isolated human and sheep umbilical vasculature.* J Pharmacol Exp Ther, 1973. **184**(2): p. 366-75.
61. Glennon, R.A., M. Titeler, and J.D. McKenney, *Evidence for 5-HT2 involvement in the mechanism of action of hallucinogenic agents.* Life Sci, 1984. **35**(25): p. 2505-11.
62. Xu, T. and S.C. Pandey, *Cellular localization of serotonin(2A) (5HT(2A)) receptors in the rat brain.* Brain Res Bull, 2000. **51**(6): p. 499-505.
63. Zonta, M., et al., *Neuron-to-astrocyte signaling is central to the dynamic control of brain microcirculation.* Nature neuroscience, 2003. **6**(1): p. 43-50.
64. Takano, T., et al., *Astrocyte-mediated control of cerebral blood flow.* Nat Neurosci, 2006. **9**(2): p. 260-7.
65. Magistretti, P.J. and L. Pellerin, *The astrocyte-mediated coupling between synaptic activity and energy metabolism operates through volume transmission.* Progress in brain research, 2000. **125**: p. 229-240.
66. Filosa, J.A. and J.A. Iddings, *Astrocyte regulation of cerebral vascular tone.* Am J Physiol Heart Circ Physiol, 2013. **305**(5): p. H609-19.
67. Attwell, D., et al., *Glial and neuronal control of brain blood flow.* Nature, 2010. **468**(7321): p. 232-43.
68. Padawer-Curry, J.A., et al., *Wide-Field Optical Imaging in Mouse Models of Ischemic Stroke.* Methods Mol Biol, 2023. **2616**: p. 113-151.
69. Ma, Y., et al., *Wide-field optical mapping of neural activity and brain haemodynamics: considerations and novel approaches.* Philos Trans R Soc Lond B Biol Sci, 2016. **371**(1705).
70. Wright, P.W., et al., *Functional connectivity structure of cortical calcium dynamics in anesthetized and awake mice.* PLoS One, 2017. **12**(10): p. e0185759.
71. Kraft, A.W., et al., *Sensory deprivation after focal ischemia in mice accelerates brain remapping and improves functional recovery through Arc-dependent synaptic plasticity.* Sci Transl Med, 2018. **10**(426).
72. Brier, L.M., et al., *Separability of calcium slow waves and functional connectivity during wake, sleep, and anesthesia.* Neurophotonics, 2019. **6**(3): p. 035002.
73. Albertson, A.J., et al., *Normal aging in mice is associated with a global reduction in cortical spectral power and network-specific declines in functional connectivity.* Neuroimage, 2022. **257**: p. 119287.
74. Silasi, G., et al., *Intact skull chronic windows for mesoscopic wide-field imaging in awake mice.* J Neurosci Methods, 2016. **267**: p. 141-9.
75. Couto, J., et al., *Chronic, cortex-wide imaging of specific cell populations during behavior.* Nat Protoc, 2021. **16**(7): p. 3241-3263.
76. Dana, H., et al., *Thy1-GCaMP6 transgenic mice for neuronal population imaging in vivo.* PLoS One, 2014. **9**(9): p. e108697.
77. Dana, H., et al., *Sensitive red protein calcium indicators for imaging neural activity.* Elife, 2016. **5**.

78. Dana, H., et al., *Thy1 transgenic mice expressing the red fluorescent calcium indicator jRGECO1a for neuronal population imaging in vivo.* PLoS One, 2018. **13**(10): p. e0205444.
79. Dana, H., et al., *High-performance calcium sensors for imaging activity in neuronal populations and microcompartments.* Nat Methods, 2019. **16**(7): p. 649-657.
80. Fosque, B.F., et al., *Neural circuits. Labeling of active neural circuits in vivo with designed calcium integrators.* Science, 2015. **347**(6223): p. 755-60.
81. Shen, Y., et al., *A genetically encoded Ca(2+) indicator based on circularly permutated sea anemone red fluorescent protein eqFP578.* BMC Biol, 2018. **16**(1): p. 9.
82. Corlu, A., et al., *Uniqueness and wavelength optimization in continuous-wave multispectral diffuse optical tomography.* Opt Lett, 2003. **28**(23): p. 2339-41.
83. Ma, Y., et al., *Resting-state hemodynamics are spatiotemporally coupled to synchronized and symmetric neural activity in excitatory neurons.* Proc Natl Acad Sci U S A, 2016. **113**(52): p. E8463-E8471.
84. Hakon, J., et al., *Multisensory stimulation improves functional recovery and resting-state functional connectivity in the mouse brain after stroke.* Neuroimage Clin, 2018. **17**: p. 717-730.
85. Quattromani, M.J., et al., *Changes in resting-state functional connectivity after stroke in a mouse brain lacking extracellular matrix components.* Neurobiol Dis, 2018. **112**: p. 91-105.
86. Bauer, A.Q., et al., *Effective Connectivity Measured Using Optogenetically Evoked Hemodynamic Signals Exhibits Topography Distinct from Resting State Functional Connectivity in the Mouse.* Cereb Cortex, 2018. **28**(1): p. 370-386.
87. Kraft, A.W., et al., *Sensory deprivation after focal ischemia in mice accelerates brain remapping and improves functional recovery through Arc-dependent synaptic plasticity.* Science translational medicine, 2018. **10**(426).
88. Park, K., et al., *Optical imaging of stimulation-evoked cortical activity using GCaMP6f and jRGECO1a.* Quant Imaging Med Surg, 2021. **11**(3): p. 998-1009.
89. Bauer, A.Q., et al., *Optical imaging of disrupted functional connectivity following ischemic stroke in mice.* Neuroimage, 2014. **99**: p. 388-401.
90. Kraft, A.W., et al., *Electrically coupled inhibitory interneurons constrain long-range connectivity of cortical networks.* Neuroimage, 2020. **215**: p. 116810.
91. Bice, A.R., et al., *Homotopic contralesional excitation suppresses spontaneous circuit repair and global network reconnections following ischemic stroke.* Elife, 2022. **11**.
92. Sherafati, A., et al., *Global motion detection and censoring in high-density diffuse optical tomography.* Hum Brain Mapp, 2020. **41**(14): p. 4093-4112.
93. Padawer-Curry, J.A., et al., *Wide-field optical imaging in mouse models of ischemic stroke*, in *Neural Repair: Methods and Protocols*. 2023, Springer US New York, NY. p. 113-151.
94. Paxinos, G. and K.B. Franklin, *Paxinos and Franklin's the mouse brain in stereotaxic coordinates*. 2019: Academic press.
95. Rosenthal, Z.P., et al., *Local Perturbations of Cortical Excitability Propagate Differentially Through Large-Scale Functional Networks.* Cereb Cortex, 2020. **30**(5): p. 3352-3369.

96. White, B.R., et al., *Imaging of functional connectivity in the mouse brain.* PLoS One, 2011. **6**(1): p. e16322.
97. White, B.R. and J.P. Culver, *Quantitative evaluation of high-density diffuse optical tomography: in vivo resolution and mapping performance.* J Biomed Opt, 2010. **15**(2): p. 026006.
98. Padawer-Curry, J.A., et al., *Variability in atlas registration of optical intrinsic signal imaging and its effect on functional connectivity analysis.* J Opt Soc Am A Opt Image Sci Vis, 2021. **38**(2): p. 245-252.
99. White, B.R., et al., *Wavelength censoring for spectroscopy in optical functional neuroimaging.* Phys Med Biol, 2021. **66**(6): p. 065026.
100. White, B.R., et al., *Brain segmentation, spatial censoring, and averaging techniques for optical functional connectivity imaging in mice.* Biomed Opt Express, 2019. **10**(11): p. 5952-5973.
101. Brier, L.M. and J.P. Culver, *An open source statistical and data processing toolbox for wide-field optical imaging in mice.* BioRxiv, 2021: p. 2021.04. 07.438885.
102. White, B.R., et al., *Controlling the familywise error rate in widefield optical neuroimaging of functional connectivity in mice.* Neurophotonics, 2023. **10**(1): p. 015004.
103. Shahar, O., et al., *Role of 5-HT2A, 5-HT2C, 5-HT1A and TAAR1 Receptors in the Head Twitch Response Induced by 5-Hydroxytryptophan and Psilocybin: Translational Implications.* International Journal of Molecular Sciences, 2022. **23**(22).
104. Jaster, A.M., et al., *Differences across sexes on head-twitch behavior and 5-HT2A receptor signaling in C57BL/6J mice.* Neuroscience Letters, 2022. **788**.
105. Sun, Y., et al., *An ontogenic study of receptor mechanisms by which acute administration of low-doses of methamphetamine suppresses DOI-induced 5-HT(2A)-receptor mediated head-twitch response in mice.* BMC Neurosci, 2022. **23**(1): p. 2.
106. Willins, D.L. and H.Y. Meltzer, *Direct injection of 5-HT2A receptor agonists into the medial prefrontal cortex produces a head-twitch response in rats.* Journal of Pharmacology and Experimental Therapeutics, 1997. **282**(2): p. 699-706.
107. Halberstadt, A.L. and M.A. Geyer, *Characterization of the head-twitch response induced by hallucinogens in mice: detection of the behavior based on the dynamics of head movement.* Psychopharmacology (Berl), 2013. **227**(4): p. 727-39.
108. Halberstadt, A.L., et al., *Correlation between the potency of hallucinogens in the mouse head-twitch response assay and their behavioral and subjective effects in other species.* Neuropharmacology, 2020. **167**: p. 107933.
109. Canal, C.E. and D. Morgan, *Head-twitch response in rodents induced by the hallucinogen 2,5-dimethoxy-4-iodoamphetamine: a comprehensive history, a re-evaluation of mechanisms, and its utility as a model.* Drug Test Anal, 2012. **4**(7-8): p. 556-76.
110. Atasoy, S., et al., *Common neural signatures of psychedelics: frequency-specific energy changes and repertoire expansion revealed using connectome-harmonic decomposition.* Progress in Brain Research, 2018. **242**: p. 97-120.
111. Celada, P., et al., *The hallucinogen DOI reduces low-frequency oscillations in rat prefrontal cortex: reversal by antipsychotic drugs.* Biol Psychiatry, 2008. **64**(5): p. 392-400.

112. Wood, J., Y. Kim, and B. Moghaddam, *Disruption of prefrontal cortex large scale neuronal activity by different classes of psychotomimetic drugs.* J Neurosci, 2012. **32**(9): p. 3022-31.
113. Tagliazucchi, E., et al., *Baseline Power of Theta Oscillations Predicts Mystical-Type Experiences Induced by DMT in a Natural Setting.* Front Psychiatry, 2021. **12**: p. 720066.
114. Valle, M., et al., *Inhibition of alpha oscillations through serotonin-2A receptor activation underlies the visual effects of ayahuasca in humans.* European Neuropsychopharmacology, 2016. **26**(7): p. 1161-1175.
115. Muthukumaraswamy, S.D., et al., *Broadband cortical desynchronization underlies the human psychedelic state.* J Neurosci, 2013. **33**(38): p. 15171-83.
116. He, B.J., *Scale-free brain activity: past, present, and future.* Trends Cogn Sci, 2014. **18**(9): p. 480-7.
117. Drew, P.J., *Neurovascular coupling: motive unknown.* Trends Neurosci, 2022. **45**(11): p. 809-819.
118. Yuan, R., et al., *Regional homogeneity of resting-state fMRI contributes to both neurovascular and task activation variations.* Magnetic Resonance Imaging, 2013. **31**(9): p. 1492-1500.
119. Devonshire, I.M., et al., *Neurovascular coupling is brain region-dependent.* Neuroimage, 2012. **59**(3): p. 1997-2006.
120. Ekstrom, A.D., *Regional variation in neurovascular coupling and why we still lack a Rosetta Stone.* Philosophical Transactions of the Royal Society B-Biological Sciences, 2021. **376**(1815).
121. Sloan, H., et al., *Regional differences in neurovascular coupling in rat brain as determined by fMRI and electrophysiology.* Neuroimage, 2010. **53**(2): p. 399-411.
122. Spain, A., et al., *Neurovascular and neuroimaging effects of the hallucinogenic serotonin receptor agonist psilocin in the rat brain.* Neuropharmacology, 2015. **99**: p. 210-20.
123. Puig, M.V., et al., *In vivo modulation of the activity of pyramidal neurons in the rat medial prefrontal cortex by 5-HT2A receptors: relationship to thalamocortical afferents.* Cereb Cortex, 2003. **13**(8): p. 870-82.
124. Williams, G.V., S.G. Rao, and P.S. Goldman-Rakic, *The physiological role of 5-HT2A receptors in working memory.* J Neurosci, 2002. **22**(7): p. 2843-54.
125. Willins, D.L., A.Y. Deutch, and B.L. Roth, *Serotonin 5-HT2A receptors are expressed on pyramidal cells and interneurons in the rat cortex.* Synapse, 1997. **27**(1): p. 79-82.
126. Bonhaus, D.W., et al., *The pharmacology and distribution of human 5-hydroxytryptamine2B (5-HT2B) receptor gene products: comparison with 5-HT2A and 5-HT2C receptors.* Br J Pharmacol, 1995. **115**(4): p. 622-8.
127. Burnet, P.W., et al., *The distribution of 5-HT1A and 5-HT2A receptor mRNA in human brain.* Brain Res, 1995. **676**(1): p. 157-68.
128. Gonzalez-Maeso, J. and S.C. Sealfon, *Psychedelics and schizophrenia.* Trends in Neurosciences, 2009. **32**(4): p. 225-232.
129. Nichols, D.E., *Chemistry and structure–activity relationships of psychedelics.* Behavioral Neurobiology of Psychedelic Drugs, 2018: p. 1-43.
130. Ray, T.S., *Psychedelics and the human receptorome.* PloS one, 2010. **5**(2): p. e9019.

131. Aznar, S. and S. Hervig Mel, *The 5-HT2A serotonin receptor in executive function: Implications for neuropsychiatric and neurodegenerative diseases.* Neurosci Biobehav Rev, 2016. **64**: p. 63-82.
132. Zhang, G. and R.W. Stackman, Jr., *The role of serotonin 5-HT2A receptors in memory and cognition.* Front Pharmacol, 2015. **6**: p. 225.
133. Savalia, N.K., L.X. Shao, and A.C. Kwan, *A Dendrite-Focused Framework for Understanding the Actions of Ketamine and Psychedelics.* Trends Neurosci, 2021. **44**(4): p. 260-275.
134. Kometer, M., et al., *Activation of serotonin 2A receptors underlies the psilocybin-induced effects on alpha oscillations, N170 visual-evoked potentials, and visual hallucinations.* J Neurosci, 2013. **33**(25): p. 10544-51.
135. Timmermann, C., et al., *Human brain effects of DMT assessed via EEG-fMRI.* Proc Natl Acad Sci U S A, 2023. **120**(13): p. e2218949120.
136. Alamia, A., et al., *DMT alters cortical travelling waves.* Elife, 2020. **9**.
137. Davies, M.F., et al., *Two distinct effects of 5-hydroxytryptamine on single cortical neurons.* Brain Res, 1987. **423**(1-2): p. 347-52.
138. Araneda, R. and R. Andrade, *5-Hydroxytryptamine2 and 5-hydroxytryptamine 1A receptors mediate opposing responses on membrane excitability in rat association cortex.* Neuroscience, 1991. **40**(2): p. 399-412.
139. Kwan, A.C., et al., *The neural basis of psychedelic action.* Nat Neurosci, 2022. **25**(11): p. 1407-1419.
140. Girn, M., et al., *A complex systems perspective on psychedelic brain action.* Trends Cogn Sci, 2023. **27**(5): p. 433-445.
141. McCulloch, D.E., et al., *Psychedelic resting-state neuroimaging: A review and perspective on balancing replication and novel analyses.* Neurosci Biobehav Rev, 2022. **138**: p. 104689.
142. Gattuso, J.J., et al., *Default Mode Network Modulation by Psychedelics: A Systematic Review.* Int J Neuropsychopharmacol, 2023. **26**(3): p. 155-188.
143. Rostrup, E., et al., *Functional MRI of CO2 induced increase in cerebral perfusion.* NMR Biomed, 1994. **7**(1-2): p. 29-34.
144. Puig, M.V. and A.T. Gulledge, *Serotonin and prefrontal cortex function: neurons, networks, and circuits.* Mol Neurobiol, 2011. **44**(3): p. 449-64.
145. Andrade, R., *Serotonergic regulation of neuronal excitability in the prefrontal cortex.* Neuropharmacology, 2011. **61**(3): p. 382-6.
146. Cauli, B., et al., *Cortical GABA interneurons in neurovascular coupling: relays for subcortical vasoactive pathways.* J Neurosci, 2004. **24**(41): p. 8940-9.
147. Schmitz, G.P., et al., *Psychedelic compounds directly excite 5-HT2A Layer 5 Pyramidal Neurons in the Prefrontal Cortex through a 5-HT2A Gq-mediated activation mechanism.* bioRxiv, 2022: p. 2022.11. 15.516655.
148. Cohen, Z., et al., *Serotonin in the regulation of brain microcirculation.* Prog Neurobiol, 1996. **50**(4): p. 335-62.
149. López-Giménez, J.F. and J. González-Maeso, *Hallucinogens and serotonin 5-HT 2A receptor-mediated signaling pathways.* Behavioral Neurobiology of Psychedelic Drugs, 2018: p. 45-73.

150. Haydon, P.G. and G. Carmignoto, *Astrocyte control of synaptic transmission and neurovascular coupling.* Physiol Rev, 2006. **86**(3): p. 1009-31.
151. Rosenegger, D.G. and G.R. Gordon, *A slow or modulatory role of astrocytes in neurovascular coupling.* Microcirculation, 2015. **22**(3): p. 197-203.
152. Petzold, G.C. and V.N. Murthy, *Role of astrocytes in neurovascular coupling.* Neuron, 2011. **71**(5): p. 782-97.
153. Griffith, S., J. Lincoln, and G. Burnstock, *Serotonin as a neurotransmitter in cerebral arteries.* Brain Research, 1982. **247**(2): p. 388-392.
154. Watts, S.W., et al., *Serotonin and blood pressure regulation.* Pharmacol Rev, 2012. **64**(2): p. 359-88.
155. Liu, T.T., *Noise contributions to the fMRI signal: An overview.* Neuroimage, 2016. **143**: p. 141-151.
156. Cardenas, D.P., et al., *Functional MRI during hyperbaric oxygen: effects of oxygen on neurovascular coupling and BOLD fMRI signals.* Neuroimage, 2015. **119**: p. 382-389.
157. Weckesser, M., et al., *Functional imaging of the visual cortex with bold-contrast MRI: hyperventilation decreases signal response.* Magn Reson Med, 1999. **41**(1): p. 213-6.
158. Rostrup, E., et al., *Regional differences in the CBF and BOLD responses to hypercapnia: a combined PET and fMRI study.* Neuroimage, 2000. **11**(2): p. 87-97.
159. Phillips, A.A., et al., *Neurovascular coupling in humans: Physiology, methodological advances and clinical implications.* J Cereb Blood Flow Metab, 2016. **36**(4): p. 647-64.
160. Schmid, Y., et al., *Acute Effects of Lysergic Acid Diethylamide in Healthy Subjects.* Biol Psychiatry, 2015. **78**(8): p. 544-53.
161. Palenicek, T., et al., *Behavioral, neurochemical and pharmaco-EEG profiles of the psychedelic drug 4-bromo-2,5-dimethoxyphenethylamine (2C-B) in rats.* Psychopharmacology (Berl), 2013. **225**(1): p. 75-93.
162. Halberstadt, A.L., F.X. Vollenweider, and D.E. Nichols, *Behavioral neurobiology of psychedelic drugs*. Vol. 36. 2018: Springer.
163. Jobst, B.M., et al., *Increased sensitivity to strong perturbations in a whole-brain model of LSD.* Neuroimage, 2021. **230**: p. 117809.
164. Siegel, J.S., et al., *Psilocybin desynchronizes brain networks.* medRxiv, 2023.
165. Jenkins, G.M., *Spectral analysis and its applications.* Holden-Day, Inc., San Francisco, Card Nr. 67-13840, 1968.
166. Kim, K.J., et al., *Vasculo-Neuronal Coupling: Retrograde Vascular Communication to Brain Neurons.* J Neurosci, 2016. **36**(50): p. 12624-12639.
167. Moore, C.I. and R. Cao, *The hemo-neural hypothesis: on the role of blood flow in information processing.* J Neurophysiol, 2008. **99**(5): p. 2035-47.
168. Gao, Y.R., et al., *Time to wake up: Studying neurovascular coupling and brain-wide circuit function in the un-anesthetized animal.* Neuroimage, 2017. **153**: p. 382-398.
169. Shmuel, A., et al., *Negative functional MRI response correlates with decreases in neuronal activity in monkey visual area V1.* Nat Neurosci, 2006. **9**(4): p. 569-77.
170. Vollenweider, F.X., et al., *Positron emission tomography and fluorodeoxyglucose studies of metabolic hyperfrontality and psychopathology in the psilocybin model of psychosis.* Neuropsychopharmacology, 1997. **16**(5): p. 357-372.

171. Gorrostieta, C., et al., *Investigating brain connectivity using mixed effects vector autoregressive models.* Neuroimage, 2012. **59**(4): p. 3347-55.
172. Friston, K., *Causal modelling and brain connectivity in functional magnetic resonance imaging.* PLoS Biol, 2009. **7**(2): p. e33.
173. Raut, R.V., et al., *Global waves synchronize the brain's functional systems with fluctuating arousal.* Sci Adv, 2021. **7**(30).
174. Jafarian, A., et al., *Comparing dynamic causal models of neurovascular coupling with fMRI and EEG/MEG.* Neuroimage, 2020. **216**: p. 116734.
175. Pokorny, T., et al., *Modulatory effect of the 5-HT1A agonist buspirone and the mixed non-hallucinogenic 5-HT1A/2A agonist ergotamine on psilocybin-induced psychedelic experience.* Eur Neuropsychopharmacol, 2016. **26**(4): p. 756-66.
176. Lambe, E.K. and G.K. Aghajanian, *Prefrontal cortical network activity: Opposite effects of psychedelic hallucinogens and D1/D5 dopamine receptor activation.* Neuroscience, 2007. **145**(3): p. 900-10.
177. Stahl, S.M., *Beyond the dopamine hypothesis of schizophrenia to three neural networks of psychosis: dopamine, serotonin, and glutamate.* CNS Spectr, 2018. **23**(3): p. 187-191.
178. Inserra, A., *Hypothesis: The Psychedelic Ayahuasca Heals Traumatic Memories via a Sigma 1 Receptor-Mediated Epigenetic-Mnemonic Process.* Front Pharmacol, 2018. **9**: p. 330.
179. Jinks, T. and T. Jinks, *The How and Why of Psychedelics.* Psychological Perspectives on Reality, Consciousness and Paranormal Experience, 2019: p. 179-190.
180. Cao, D., et al., *Structure-based discovery of nonhallucinogenic psychedelic analogs.* Science, 2022. **375**(6579): p. 403-411.
181. Cameron, L.P., et al., *A non-hallucinogenic psychedelic analogue with therapeutic potential.* Nature, 2021. **589**(7842): p. 474-479.
182. Qu, Y., et al., *Rapid antidepressant-like effect of non-hallucinogenic psychedelic analog lisuride, but not hallucinogenic psychedelic DOI, in lipopolysaccharide-treated mice.* Pharmacol Biochem Behav, 2023. **222**: p. 173500.
183. Wise, R.G. and I. Tracey, *The role of fMRI in drug discovery.* J Magn Reson Imaging, 2006. **23**(6): p. 862-76.
184. Menon, V., et al., *Combined event-related fMRI and EEG evidence for temporal-parietal cortex activation during target detection.* Neuroreport, 1997. **8**(14): p. 3029-37.
185. Centeno, M. and D.W. Carmichael, *Network Connectivity in Epilepsy: Resting State fMRI and EEG-fMRI Contributions.* Front Neurol, 2014. **5**: p. 93.
186. Hathout, G.M., et al., *The lag of cerebral hemodynamics with rapidly alternating periodic stimulation: modeling for functional MRI.* Magn Reson Imaging, 1999. **17**(1): p. 9-20.
187. Anderson, J.S., *Origin of synchronized low-frequency blood oxygen level-dependent fluctuations in the primary visual cortex.* AJNR Am J Neuroradiol, 2008. **29**(9): p. 1722-9.
188. Eggebrecht, A.T., et al., *Mapping distributed brain function and networks with diffuse optical tomography.* Nat Photonics, 2014. **8**(6): p. 448-454.
189. Eggebrecht, A.T., et al., *A quantitative spatial comparison of high-density diffuse optical tomography and fMRI cortical mapping.* Neuroimage, 2012. **61**(4): p. 1120-8.
190. Lu, H., S. Jaime, and Y. Yang, *Origins of the Resting-State Functional MRI Signal: Potential Limitations of the "Neurocentric" Model.* Front Neurosci, 2019. **13**: p. 1136.

191. Volterra, A., N. Liaudet, and I. Savtchouk, *Astrocyte Ca(2)(+) signalling: an unexpected complexity.* Nat Rev Neurosci, 2014. **15**(5): p. 327-35.
192. Perea, G. and A. Araque, *GLIA modulates synaptic transmission.* Brain Res Rev, 2010. **63**(1-2): p. 93-102.
193. Bazargani, N. and D. Attwell, *Astrocyte calcium signaling: the third wave.* Nat Neurosci, 2016. **19**(2): p. 182-9.
194. Aronov, D. and M.S. Fee, *Natural changes in brain temperature underlie variations in song tempo during a mating behavior.* PLoS One, 2012. **7**(10): p. e47856.

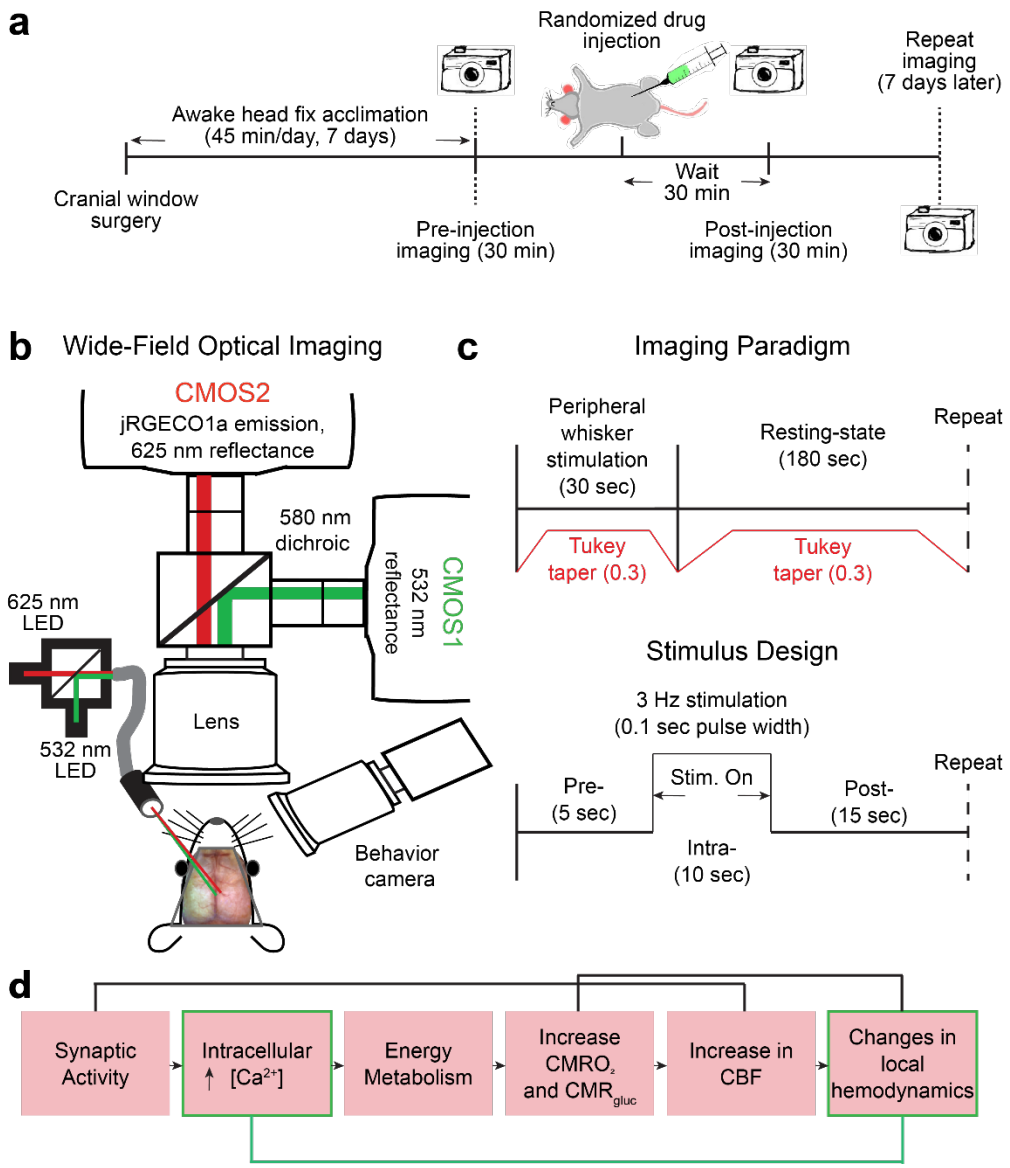

Figure 1) Measuring the effect of $5HT_{2a}$ receptor agonism on cortical-wide wide neurovascular coupling using wide-field optical imaging. 8 Thy1-jRGECO1a mice (4 male, 4 female) were used for experimentation**. a) Experimental timeline**. Prior to imaging, a cranial window was secured to the intact skull followed by 3 days of recovery. Mice were acclimated to head fixed WFOI apparatus for 7 days, 45 minutes per day. Mice were randomly assigned to different drugs conditions, and all drugs were prepared the day of experimentation. Mice were imaged for ~30 minutes prior to drug injection. After injection of drugs (delivered i.p., 20ml/kg), mice were allowed 30 minutes for the drug to take effect, followed by ~30 minutes of WFOI. After one week, this process was repeated for the remaining 2 drugs for a total of 3 WFOI sessions per mouse. **b) Schematic of WFOI system**. A custom light engine consisting of 530 nm and 625 nm LEDs illuminated the skull. Fluorescence emission and diffuse reflected light were collected by a lens, split by a 580 nm dichroic, and sampled by two sCMOS cameras. A 500 nm long pass filter in front of CMOS1 passed 530 nm reflectance while the dichroic and a 590 nm long pass filter in front of CMOS2 passed jRGECO1a emission and 625 nm reflectance. A second 700 nm long pass filter in front of CMOS2 blocked near infrared light used for movement monitoring (see below). **c) Imaging paradigm**. Epochs of awake peripheral whisker stimulation were interwoven with awake resting-state imaging. Imaging consisted of stimulus blocks of 10 seconds of air puffs (40 PSI, 100 ms pulses delivered at 3 Hz) followed by 20 seconds of recovery then 180 seconds of rest. This paradigm was repeated 9 times per imaging condition (*i.e.*, 31.5 minutes of baseline imaging, and 31.5 minutes during the effects of a drug). Stimulus evoked

responses and resting-state activity were temporally windowed using a Tukey window (with lobe parameter of 0.3) to minimize boundary effects. **d) Simplified illustration of neurovascular coupling (NVC).** During increased synaptic activity (neural activity), voltage-gated calcium (Ca2+) channels initiate action potential propagation along the cell surface membrane resulting in increased intracellular calcium concentration changes, detectable using the red-shifted genetically encoded calcium indicator (GECI), jRGECO1a. Changes in neuronal activity are sufficient to drive changes in cerebral blood flow, as well as blood oxygenation. Local changes in energy metabolism, associated with resetting membrane potentials and other events, happen on the order of 10s to 100s of milliseconds. In parallel, increases in the cerebral metabolic rate of oxygen ($CMRO_2$) and glucose (CMR_{gluc}) also result in local changes in blood oxygenation from increasesd blood volume and/or blood flow. These latter processes happen on the order of seconds. WFOI captures the correspondence between calcium concentration changes and subsequent changes in blood volume and oxygenation.

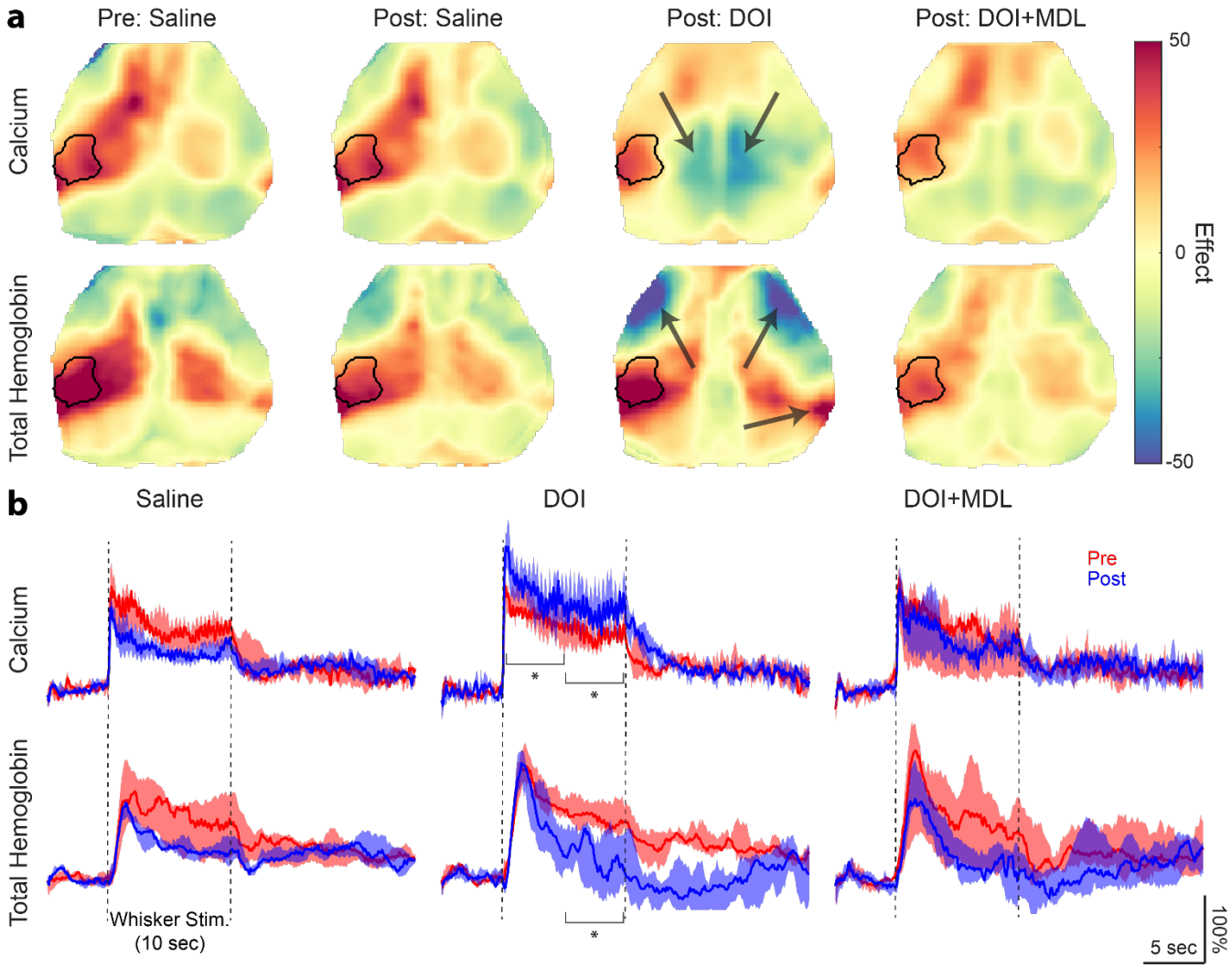

Figure 2) DOI differentially alters calcium and hemodynamic stimulus responses. Peripheral whisker stimulation was delivered *via* air puffs (40 pounds-per-square-inch) on the right whiskers for 10 seconds at 3 Hz (100 msec pulses). Each session (*i.e.*, pre-injection and post-injection) resulted in 9 stimulus presentations. All calcium movies before injection were averaged and a region of interest (ROI, in solid black) was extracted and used for subsequent analysis (**Fig. S2a**). Large black arrows indicate where there were large alterations in topography, which have been quantified by spatial correlations. **a) Stimulus response effect maps.** The effect (Cohen's D) at each pixel was calculated between the pre-stimulus and the contrast-specific intra-stimulus period, which to control for fixed effects, was chosen as 5 seconds in length. To assess differential changes in stimulus-response topography of calcium versus hemodynamics, spatial correlations were calculated. DOI decreased spatial correlations between calcium and hemodynamic response topography (-0.45 [-0.63, -0.28], Kruskal-Wallis, p=0.010, DOI versus saline, p=0.008). DOI decreased calcium responses within the ROI (-25.72% [-32.4%, -6.52%], pre-versus post-injection, p=0.031, Kruskal-Wallis, p=0.374). In contrast, hemodynamic response effects were not differentially altered by drug (Kruskal-Wallis, p=0.643). **b) Stimulus response dynamics.** Pixel time courses within the ROI were averaged and visualized as medians and 25th and 75th. Both calcium and hemodynamic responses were normalized by their maximum reponse magnitude before injection for display purposes. DOI increased both the calcium peak (26.0% [24.2%, 63.2%], p=0.031) and sustained responses (40.0% [3.4%, 120.7%], p=0.031). In contrast, hemodynamic sustained responses decreased after both DOI (-70.3% [-132.3%, -39.5%], p=0.031) and DOI+MDL (-93.6 [-138.5%, 56.6%], p=0.031). DOI also decreased hemodynamic response effect (-38.8% [-63.1%, -24.0%], p=0.031).

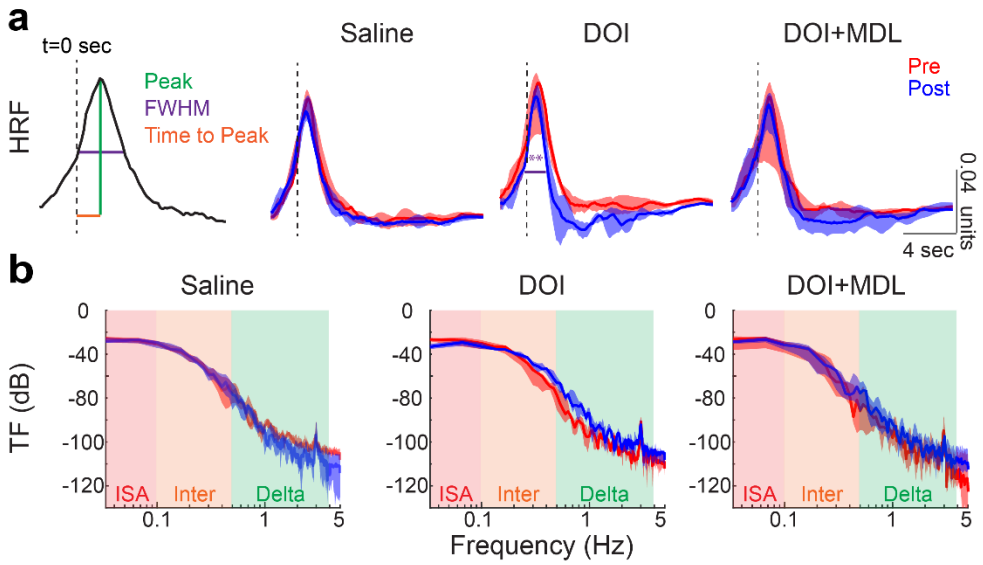

Figure 3) 5-HT$_{2a}$ receptor agonism alters task-based neurovascular coupling. a) Task-based hemodynamic response functions. Neurovascular coupling was assessed using the stimulus evoked responses in Figure 2b, and hemodynamic response functions (HRFs) were estimated using a weighted least squares deconvolution method. A 3 second delay between calcium and hemodynamics examined potential quasi-acausal relationships prior to time zero (dotted black line, when Calcium and HbT are temporally aligned). The y-axis has units of μMol/(ΔF/F%). Group-level averages before and after drug injection are displayed and presented as medians and 25th and 75th percentiles across mice. HRFs were parametrized using peak value (peak, green), time to peak (TTP, orange), and full width at half maximum (FWHM, purple) for each session, mouse, and drug. The effect of drug (*i.e.*, post versus pre) was determined using Wilcoxon's sign-rank tests (*<0.05, **<0.01, ***<0.001). DOI significantly decreased the FWHM of the HRF (-31.4% [-36.0%, -27.8%], p=0.031, Kruskal-Wallis, p=0.027, saline versus DOI, p=0.028). **b) Task-based transfer functions.** To better understand the frequency content present in the HRFs, transfer functions were calculated as the power spectral density of the HRF and are presented as medians and 25th and 75th percentiles across mice. To calculate transduction, transfer functions (TF) were integrated over ISA (0.03-0.08 Hz), intermediate (0.08-0.50 Hz), and delta (0.5-4.0 Hz) frequency ranges. The y-axis has units of $(\mu\text{Mol}/(\Delta F/F\%))^2/\text{Hz}$. Following DOI administration, there was a trend of increased transduction in frequencies above 0.5 Hz (delta band increase +367% [57%, 472%], p=0.063).

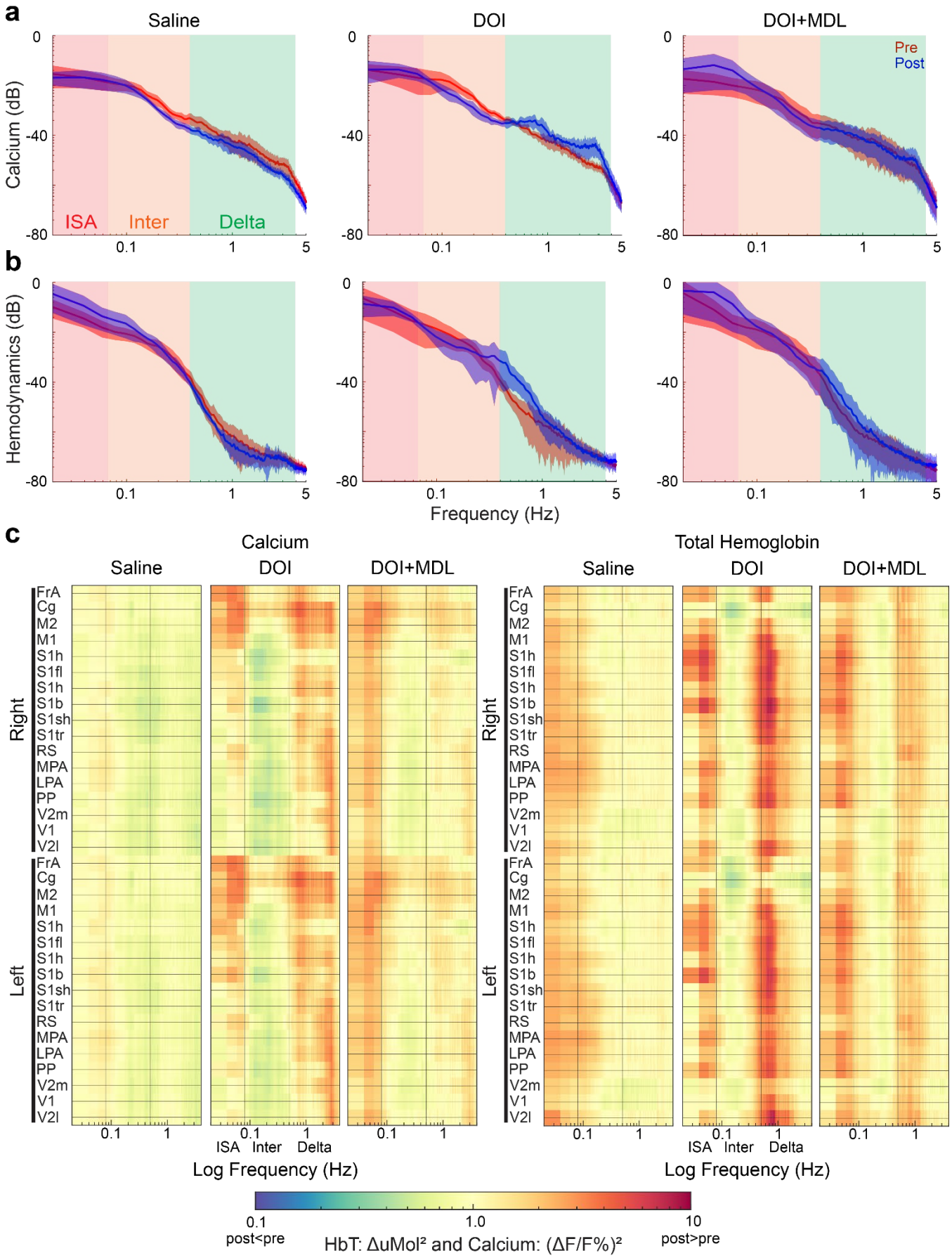
a
Saline
DOI
DOI+MDL
Pre
Post
Calcium (dB)
ISA
Inter
Delta
b
Hemodynamics (dB)
Frequency (Hz)
c
Calcium
Total Hemoglobin
Saline
DOI
DOI+MDL
Right
Left
FrA
Cg
M2
M1
S1h
S1fl
S1h
S1b
S1sh
S1tr
RS
MPA
LPA
PP
V2m
V1
V2l
Log Frequency (Hz)
post<pre
post>pre
HbT: ΔuMol² and Calcium: (ΔF/F%)²

Figure 4) 5-HT_{2a} receptor agonism differentially modulates local and global resting-state neuronal and hemodynamic activity. Power spectral density estimates were calculated for resting-state epochs of (**a**) calcium and (**b**) hemodynamic activity and averaged across all cortical regions to obtain a cortical-wide (*i.e.*, global) power spectral density estimate. Group-level averages are displayed as means and standard deviations across mice. **A) Power spectral density estimates of calcium activity.** After DOI, calcium power decreased between 0.08 Hz and 0.64 Hz (0.08 Hz-0.32 Hz, p=0.009 and 0.16 Hz-0.64 Hz, p=0.020), but increased in power above 0.32 Hz (ANOVA and saline versus DOI post-hoc; 0.32 Hz-1.28 Hz, p=0.0006 and p=0.0005; 0.64 Hz-2.56 Hz, p=0.0018 and p=0.0007; 1.28 Hz-5.15 Hz, p=0.0017 and p=0.0013). In contrast to saline and DOI, DOI+MDL largely preserved pre-injection power spectral characteristics (increased only over 0.02 Hz-0.08 Hz, p=0.018, and 0.04 Hz-0.16 Hz, p=0.008). **b) Power spectral density estimates of hemodynamic activity.** In contrast to neuronal activity, global hemodynamic activity revealed distinct changes. Following saline, hemodynamic power increased in lower frequencies (0.02 Hz-0.08 Hz, p=0.045; 0.04 Hz-0.16 Hz, p=0.044). As observed in calcium, DOI increased lower delta-band frequencies (0.32 Hz-1.28 Hz, p=0.002, ANOVA p<0.0001 and post-hoc DOI vs saline p<0.0001; 0.64 Hz-2.56 Hz, p=0.006, ANOVA p<0.0001 and post-hoc DOI vs saline p<0.0001). **c) Regional changes in power.** Regionally averaged calcium and hemodynamic signals were calculated over regions defined by the Paxinos atlas. Power spectral density estimates (PSDs) of calcium (left) and hemodynamic (right) activity were calculated for each regional signal. To visualize fractional changes in frequency content arising from drug administration, PSDs are displayed as the ratio of post-divided-by-pre-injection. Regional PSDs are organized in order of posterior-to-anterior and from right-to-left. Warmer colors (>1, redder) indicate regional power is greater after injection whereas cooler colors (<1, bluer) indicate reductions in power after injection. Integrated power was calculated over double octave bins and compared across groups (Fig. S3a, b). Following saline, calcium power was minimally affected. DOI differentially effected hemodynamic versus calcium power spectrum characteristics. A cortical-wide hemodynamic (right) delta-band peak emerged but was not present in cingulate and retrosplenial cortex. To a lesser degree, this feature was evident in calcium signals (left) and shifted to higher frequencies. In contrast to hemodynamic signals, calcium signals in retrosplenial and cingulate cortex were not distinguished from the rest of the cortex. In the intermediate frequencies, calcium activity decreased in all cortical regions excluding frontal and cingulate. In contrast, hemodynamic activity decreased in frontal and cingulate cortex. DOI increased calcium ISA power in frontal, cingulate, and motor cortices while hemodynamic ISA activity increased primarily in somatosensory regions. As in previously reported analysis, MDL largely reversed the effects of DOI. The topography of these effects is illustrated in Fig. S4.

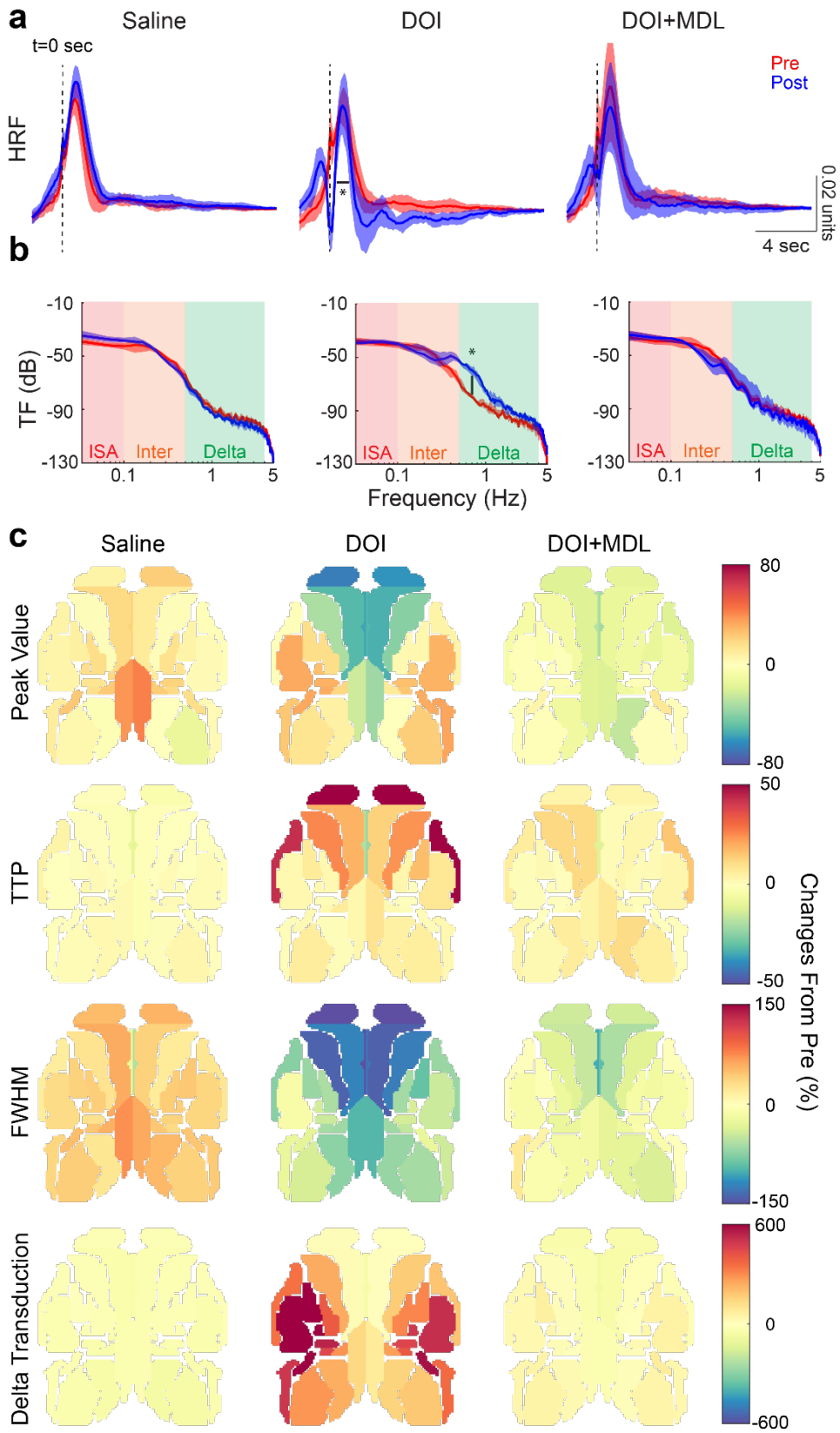

Figure 5) Elevated $5HT_{2a}$ receptor activity alters neurovascular coupling at the local and global scale. **a) Resting-state hemodynamic response functions.** Regional hemodynamic response functions

(HRF) were estimated using a weighted least squares deconvolution. A 3 second delay between calcium and hemodynamics was introduced to examine quasi-acausal relationships between calcium dynamics and hemodynamics (black dotted line indicating time zero). HRFs were averaged across all regions to obtain a global HRF. The y-axis has units of μMol/(ΔF/F%). Group-level averages (and standard deviations) before and after drug injection are displayed for each drug condition. Before drugs, resting-state HRFs resembled pre-injection task-based HRFs. On the contrary, DOI HRFs deviated from canonical form, exhibiting a peak before time zero. This feature suggests an acausal relation. Additionally, DOI increased TTP (ANOVA, p=0.020, saline versus DOI, p=0.019), reduced model fit (ANOVA p=0.040, saline versus DOI, p=0.048), and decreased FWHM (-42.7% $\pm$71.1%, p=0.015; ANOVA p=0.020, saline versus DOI, p=0.018). **b) Resting-state transfer functions.** Power spectral density estimates of the HRFs were calculated. These transfer functions are presented as mean $\pm$ standard deviation. The y-axis has units of $(\mu\text{Mol}/(\Delta F/F\%))^2$/Hz. DOI induced a quasi-oscillatory feature in lower delta frequencies (321.9%$\pm$275.2%, p=0.018, ANOVA p=0.004 saline versus DOI, p=0.004, and DOI versus DOI+MDL, p=0.028). **c) Regional neurovascular coupling.** For each regional HRF, peak value, time to peak (TTP), and full-width-at-half maximum (FWHM) were calculated. DOI induced focal, reversible NVC effects of opposite polarity in higher order association regions (*e.g.*, frontal, and cingulate) versus lateral somatosensory and parietal regions. Coupling decreased (lower peak values) in frontal/cingulate regions (-62%). More modest increases occurred in whisker-barrel cortex (32%). DOI delayed NVC (increased TTP) in frontal (51%) and anterior-lateral parts of somatomotor regions (32%). Most strikingly, DOI significantly decreased cortical-wide FWHM, most substantially in cingulate (-142%) and frontal (-183%) regions. DOI massively increased delta-band transduction (cortical-wide: 237% [79%, 350%]), except in cingulate regions (-56%). Notably, delta transduction substantially increased in the somatosensory whisker-barrel cortex (793%).

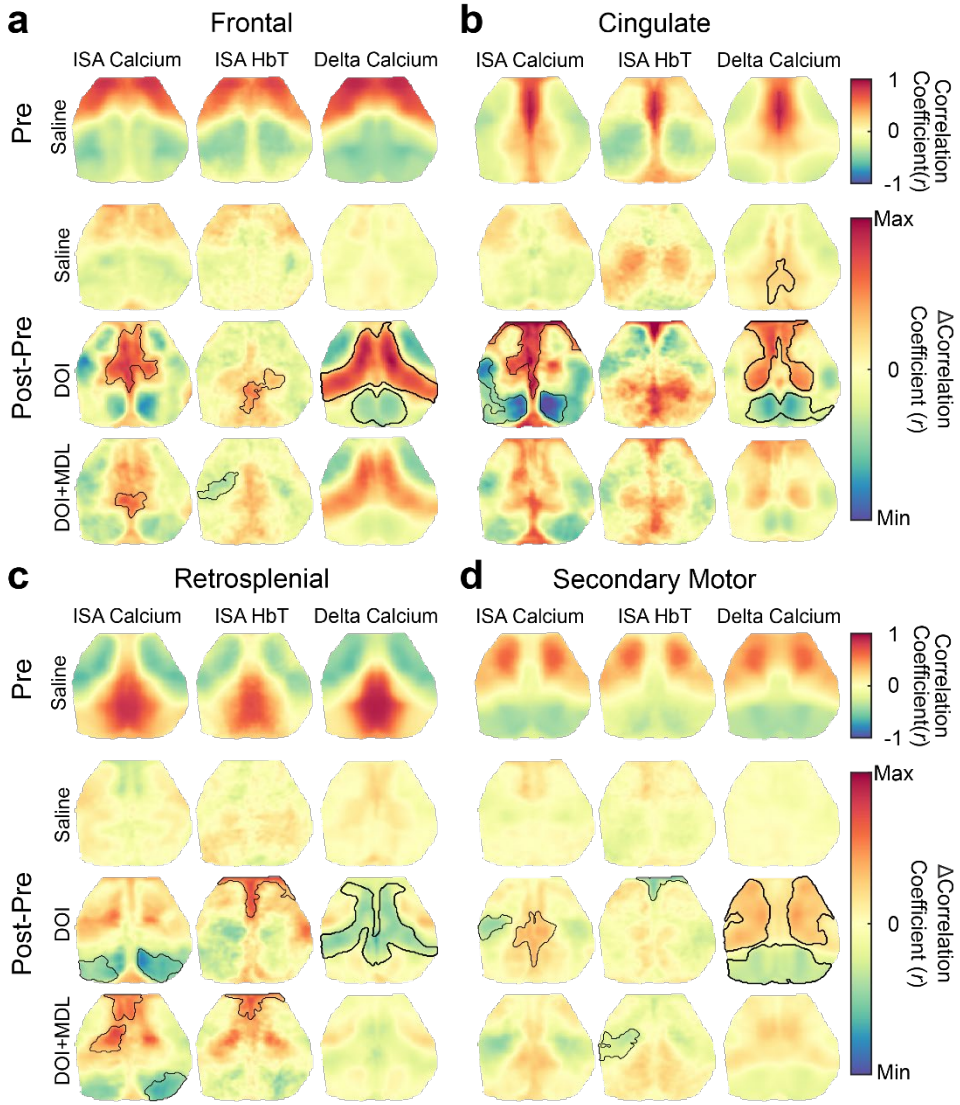

Figure 6) DOI differentially alters resting-state functional connectivity reported by calcium versus hemodynamic signals. Pairwise zero-lag correlation was calculated for each pixel within each functional region (*e.g.*, Frontal, Cingulate, Retrosplenial, and M2) determined by the Paxinos atlas before and after injection. Differences of calcium- and hemodynamic- based RSFC before and after injection were assessed (calculated as post-injection minus pre-injection in Fisher space). Statistical significance in RSFC were evaluated using cluster-based statistical analysis. Significant clusters ($p < 0.05$) are outlined in black, and the average correlation is displayed adjacently. The maximum and minimum change in correlation (as presented in the color bar) is 0.5 and 0.3 for ISA and delta bands, respectively. **a) Frontal functional connectivity.** Saline had no impact on frontal RSFC. DOI enhanced inter-network ISA calcium functional connectivity between frontal and cingulate regions ($\Delta r = +0.31 \pm 0.15$) and inter-network ISA HbT connectivity between frontal and parts of posterior retrosplenial ($\Delta r = +0.18 \pm 0.10$, middle). Additionally, DOI increased delta calcium connectivity between frontal and secondary motor/parts of posterior somatosensory ($\Delta r = +0.18 \pm 0.03$, right) and increased negative connectivity between frontal and retrosplenial regions ($\Delta r = -0.11 \pm 0.05$, right). MDL largely attenuated the effects of DOI (alterations only in ISA calcium RSFC between frontal and retrosplenial: $\Delta r = +0.20 \pm 0.13$ and ISA HbT RSFC between frontal and somatosensory: $\Delta r = -0.16 \pm 0.06$). **b) Cingulate functional connectivity.** Saline minimally elevated

delta connectivity between cingulate and retrosplenial regions (Δr = +0.07±0.05). On the contrary, DOI massively enhanced negative ISA calcium connectivity between cingulate and posterior-lateral parts of retrosplenial regions (Δr = -0.41±0.17) and strengthened calcium connectivity between cingulate/frontal and anterior-medial parts of retrosplenial regions (Δr = +0.40±0.24). All calcium observations under DOI conditions were not reflected in hemodynamic measures of ISA RSFC. DOI increased delta calcium negative connectivity strength between cingulate and retrosplenial regions (Δr = -0.14±0.07) and increased connectivity strength between cingulate and frontal and parts of medial somatosensory regions (Δr = 0.15±0.04). MDL reversed all DOI effects. **c) Retrosplenial functional connectivity.** Saline had no impact on retrosplenial RSFC. DOI decreased ISA calcium functional connectivity strength within retrosplenial cortex and between retrosplenial and lateral visual regions (left hemisphere: Δr = -0.22±0.14, right hemisphere: Δr = -0.31±0.19). Further, DOI enhanced ISA HbT functional connectivity strength between retrosplenial and frontal/cingulate regions (Δr = +0.29±0.12). MDL did not fully reverse the effects of MDL (ISA calcium change in connectivity between retrosplenial and frontal/cingulate of Δr = 0.25±0.20, between retrosplenial and medial somatosensory of Δr = 0.25±0.16, and between retrosplenial and lateral visual networks of Δr = -0.28±0.20. ISA HbT change in connectivity between retrosplenial and frontal/cingulate of Δr = 0.26±0.16.). Lastly, DOI increased negative delta calcium connectivity strength within retrosplenial cortex and between retrosplenial and secondary motor/ posterior parts of somatosensory (Δr = -0.11±0.02). **c) Secondary motor functional connectivity.** Saline had no impact on secondary motor (M2) RSFC. DOI increased negative ISA calcium functional connectivity strength between M2 and lateral somatosensory (Δr = -0.18±0.12), and increased connectivity strength between M2 and anterior cingulate/posterior retrosplenial (Δr = -0.15±0.07). This effect was not observed in hemodynamic measures of ISA RSFC (decreased connectivity between M2 and cingulate of Δr = -0.20±0.11). Additionally, delta calcium RSFC was increased between M2 and somatomotor cortex (left hemisphere: Δr = +0.09±0.03, right hemisphere: Δr = +0.09±0.05) and increased negative connectivity strength between M2 and retrosplenial/visual regions (Δr = +0.09±0.04). MDL reversed nearly all DOI effects (excluding an increased negative ISA HbT connectivity strength between M2 and somatosensory cortex).

Table 1) DOI induced topographical differences in calcium versus hemodynamic resting-state functional connectivity. Differences in correlation maps (*i.e.*, post- minus pre-injection) were calculated for each mouse, drug condition, and region (Fig. 6C). To evaluate the correspondence between calcium-versus-hemodynamic RSFC topography, spatial similarity (correlation) and linear relations (linear regression) were assessed for these RSFC difference matrices. Specifically, matrix correlations and regressions were evaluated as Pearson correlations between vectorized difference RSFC matrices and linear regressions, respectively.

	Frontal	**Cingulate**	**Retrosplenial**	**M2**
Saline	y=0.53x+0.01; r=0.61	y=0.05x+0.02; r=0.05	y=0.38x+0.01; r=0.49	y=0.43x+0.00; r=0.34
DOI	y=0.46x+0.00; r=0.29	y=0.06x+0.01; r=0.05	y=0.06x+0.02; r=0.05	y=0.29x+0.02; r=0.06
DOI+MDL	y=0.56x+0.00; r=0.37	y=0.54x+0.01; r=0.45	y=0.59x+0.00; r=0.31	y=0.82x+0.00; r=0.41